Cell Reports

Two-step fitness selection for intra-host variations in SARS-CoV-2

Graphical abstract

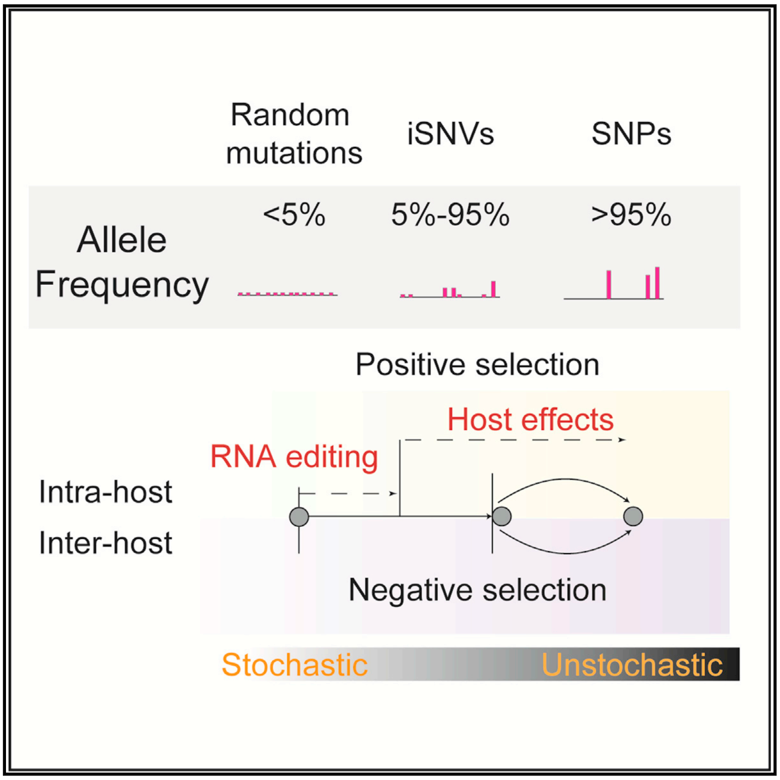

Highlights

- Intra-host variations provide a mutational pool for rapid evolution of SARS-CoV-2
- Two-step selection contributes to accumulation of intra-host variations
- iSNVs in SARS-CoV-2 display positive selection longitudinally in individuals
- The transmission bottleneck removes nonsynonymous mutations from viral population

Authors

Jiarui Li, Pengcheng Du, Lijiang Yang, ..., Jianbin Wang, Hui Zeng, Chen Chen

Correspondence

treatment@chinaaids.cn (F.Z.),
gaoyq@pku.edu.cn (Y.Q.G.),
yanyi@pku.edu.cn (Y.H.),
jianbinwang@tsinghua.edu.cn (J.W.),
zenghui@ccmu.edu.cn (H.Z.),
chenchen1@ccmu.edu.cn (C.C.)

In brief

Intra-host variations in SARS-CoV-2 provide a mutational pool shaping the rapid global evolution of the virus. Li et al. illustrate dynamic changes of iSNVs in a longitudinal cohort and explore a two-step fitness selection process of within-host viral evolution.

Li et al., 2022, Cell Reports *38*, 110205
January 11, 2022 © 2021 The Authors.
https://doi.org/10.1016/j.celrep.2021.110205

Cell Reports

CellPress
OPEN ACCESS

Article

Two-step fitness selection for intra-host variations in SARS-CoV-2

Jiarui Li,[1,2,14] Pengcheng Du,[1,2,14] Lijiang Yang,[3,4,14] Ju Zhang,[1,2,14] Chuan Song,[1,2,14] Danying Chen,[1,2,14] Yangzi Song,[1,2] Nan Ding,[1,2] Mingxi Hua,[1,2] Kai Han,[1,2] Rui Song,[1] Wen Xie,[1] Zhihai Chen,[1] Xianbo Wang,[1] Jingyuan Liu,[1] Yanli Xu,[1] Guiju Gao,[1] Qi Wang,[1] Lin Pu,[1] Lin Di,[4,5,6] Jie Li,[7] Jinglin Yue,[8] Junyan Han,[1,2] Xuesen Zhao,[1,2] Yonghong Yan,[1,2] Fengting Yu,[1] Angela R. Wu,[9,10] Fujie Zhang,[1,*] Yi Qin Gao,[3,4,11,*] Yanyi Huang,[3,4,5,6,12,*] Jianbin Wang,[7,12,*] Hui Zeng,[13,*] and Chen Chen[13,15,*]

[1]Beijing Ditan Hospital, Capital Medical University, Beijing 100015, P. R. China
[2]Beijing Key Laboratory of Emerging Infectious Diseases, Beijing 100015, P. R. China
[3]Beijing National Laboratory for Molecular Sciences, College of Chemistry and Molecular Engineering, Peking University, Beijing 100871, China
[4]Beijing Advanced Innovation Center for Genomics, Biomedical Pioneering Innovation Center, Peking University, Beijing 100871, China
[5]School of Life Sciences, Peking-Tsinghua Center for Life Sciences, Peking University, Beijing 100871, China
[6]Institute for Cell Analysis, Shenzhen Bay Laboratory, Shenzhen 518055, China
[7]School of Life Sciences, Tsinghua-Peking Center for Life Sciences, Beijing Advanced Innovation Center for Structural Biology, Tsinghua University, Beijing 100084, China
[8]Peking University Ditan Teaching Hospital, Beijing 100015, China
[9]Division of Life Science, Hong Kong University of Science and Technology, Hong Kong SAR, P.R. China
[10]Department of Chemical and Biological Engineering, Hong Kong University of Science and Technology, Hong Kong SAR, P.R. China
[11]Institute of Systems and Physical Biology, Shenzhen Bay Laboratory, Shenzhen 518055, China
[12]Chinese Institute for Brain Research, Beijing 102206, China
[13]Biomedical Innovation Center, Beijing Shijitan Hospital, Capital Medical University, Beijing 100038, China
[14]These authors contributed equally
[15]Lead contact
*Correspondence: treatment@chinaaids.cn (F.Z.), gaoyq@pku.edu.cn (Y.Q.G.), yanyi@pku.edu.cn (Y.H.), jianbinwang@tsinghua.edu.cn (J.W.), zenghui@ccmu.edu.cn (H.Z.), chenchen1@ccmu.edu.cn (C.C.)

https://doi.org/10.1016/j.celrep.2021.110205

SUMMARY

Spontaneous mutations introduce uncertainty into coronavirus disease 2019 (COVID-19) control procedures and vaccine development. Here, we perform a spatiotemporal analysis on intra-host single-nucleotide variants (iSNVs) in 402 clinical samples from 170 affected individuals, which reveals an increase in genetic diversity over time after symptom onset in individuals. Nonsynonymous mutations are overrepresented in the pool of iSNVs but underrepresented at the single-nucleotide polymorphism (SNP) level, suggesting a two-step fitness selection process: a large number of nonsynonymous substitutions are generated in the host (positive selection), and these substitutions tend to be unfixed as SNPs in the population (negative selection). Dynamic iSNV changes in subpopulations with different gender, age, illness severity, and viral shedding time displayed a varied fitness selection process among populations. Our study highlights that iSNVs provide a mutational pool shaping the rapid global evolution of the virus.

INTRODUCTION

Despite global emergence of various innovative prevention and control responses, severe acute respiratory syndrome coronavirus 2 (SARS-CoV-2) continues to spread rapidly around the world (Coronaviridae Study Group of the International Committee on Taxonomy of Viruses, 2020). Like other single-stranded RNA viruses, SARS-CoV-2 has a high mutation rate, and unexpected mutations may change the virus and make it harder to control, leading to reduced vaccine efficacy (Korber et al., 2020; Li et al., 2020). Researchers have identified numerous mutations in SARS-CoV-2 based on more than 5,000,000 published genomes (Shu and McCauley, 2017), and these mutations result in a rapid increase in PANGOLIN (phylogenetic assignment of named global outbreak lineages) (Rambaut et al., 2020), including B.1.1.7 (alpha), B.1.617.2 (delta), and, more recently, B.1.1.529 (omicron) (Jhun et al., 2021; Gao et al., 2021). Therefore, tracking SARS-CoV-2 mutations in lineages is a global monitoring priority.

Viral mutations initiate randomly in a small fraction of viruses in a single infected host and generate intra-host single-nucleotide variants (iSNVs). Some iSNVs may be subsequently fixed in hosts and transmitted among populations or transmitted as an unfixed form, and finally generate genetically diverse populations. As the virus spreads, the iSNVs are fixed through a stochastic process (e.g., genetic drift) (McCrone et al., 2018) and a deterministic process (e.g., fitness selection) (Forni et al., 2016). With high-throughput sequencing, we can explore these processes and measure genetic diversity at the population and within-host levels. Previous population-level studies using clinical, molecular, and immunological data related to single-nucleotide polymorphisms (SNPs) have provided significant insight into epidemiology and disease transmission as well as aspects of pathogenesis (Gudbjartsson et al., 2020; Tang et al., 2020).

As a larger genetic mutation pool compared with SNPs, iSNVs provide additional information defining the diversity and dynamics of viral evolution in individual hosts (Holmes et al., 2016). Analysis of iSNVs complements conventional population-level SNP studies and facilitates a more comprehensive understanding of viral evolution, which aids clinically relevant predictions of viral evolution associated with infection, pandemics, and immune evasion (McCrone et al., 2018). However, few studies have explored the genetic characteristics of iSNVs in individuals with coronavirus disease 2019 (COVID-19) (Lythgoe et al., 2021).

In the present study, we quantitatively assessed the genetic diversity of SARS-CoV-2 and viral evolution in individual hosts using deep viral genome sequencing (Chen et al., 2020) and empirical analysis pipelines (Ni et al., 2016). A spatiotemporal analysis of genomic data revealed that within-host variation was not distributed randomly throughout the genome and that such variation increased the genetic diversity of SARS-CoV-2, suggesting a role of selection. Non-synonymous mutations were overrepresented in the pool of iSNVs (mutation allele frequency [MuAF], >5% and <95%) but underrepresented in the set of SNPs (MuAF, >95%), indicating a two-step fitness selection process. We also explored the effects of iSNVs (unfixed mutation) on clinical characteristics and the binding affinity of the spike (S) protein, which might account for the observed directional selection process. Our results suggest that it is important to simultaneously study the within- and between-host dynamics of emerging viruses to understand their evolutionary histories and thus direct efforts toward developing effective methods of prevention and control.

RESULTS

Identification of intra-host variations in SARS-CoV-2 genomes

We collected 537 (183 pharyngeal, 241 sputum, and 113 fecal) samples from 204 affected individuals, covering 34.4% of total cases diagnosed in Beijing before April 30, 2020 (Figure 1A; Table S1). Using targeted capture viral genome sequencing, we obtained 8.59G base-pair (inter-quartile range [IQR], 3.12G–17.38G) per sample on average, of which 11.90% (IQR, 1.32%–53.92%) were mapped to the SARS-CoV-2 reference genome Wuhan-Hu-1 (accession number: NC_045512.2; Wu et al., 2020). Samples with low viral genomic coverage were removed (STAR Methods), and eventually 402 (136 pharyngeal swab, 182 sputum, and 84 fecal) samples from 170 affected individuals were selected for further analysis (Figure S1A). The sequencing depth was 28,720× across the genome (IQR, 4,815–46,343; Figure S1B). Among these individuals, 81 had at least two different sample types or collection time points (Figure 1B).

For each sample, we performed a high-depth (100× as the minimum depth) search of SARS-CoV-2 genomic sites for iSNVs, which were filtered using a stringent threshold ($\geq$5%) that sufficiently distinguished true iSNVs from sequencing errors (STAR Methods; supplemental information). We validated the sample processing pipeline with technical replicates in 62 samples with independent library preparation. Under the 5% cutoff for MuAF, we identified 450 reproducible iSNVs among 498 iSNVs in the first experiments. The iSNVs meeting this stringent threshold were distributed widely throughout the genome, and the number of iSNVs in each sample was not affected by genomic coverage or sequencing depth (R-square [R^2] for iSNV number and genomic coverage, 0.074; R^2 for iSNV number and sequencing depth, 0.006) (Figure S1C). In total, we identified 7,037 iSNVs in 374 samples with a median density of 0.53 iSNVs/kb, which is comparable with the number of iSNVs reported previously for SARS-CoV-2 (Lythgoe et al., 2021) and in other virus, such as Ebola virus (Ni et al., 2016), yellow fever virus (Chen et al., 2018), and influenza A virus (Debbink et al., 2017) (Table S2). About 93% of samples (374 of 402) harbored at least one iSNV in comparison with the reference genome (Table S3).

Uneven distribution of intra-host variations in SARS-CoV-2 genomes

We examined the locations of iSNVs along the SARS-CoV-2 genome and found an overall relatively low density of iSNVs (0.58 iSNVs/kb), which is comparable with previous reports (Lythgoe et al., 2021; Popa et al., 2020). Higher iSNV density was observed in the 5′ UTR (1.23 iSNVs/kb) and 3′ UTR (1.07 iSNVs/kb) (Figure 1C). We found 6,790 (96.49%) iSNVs in coding regions, which account for 97.85% of the whole genome (29,261 of 29,903). Most iSNVs (4,625, 68.11%) were identified in open reading frame (ORF) 1ab, followed by the S gene (903 iSNVs) and N gene (459 iSNVs) (Figure S1D). However, after we normalized iSNVs for gene length, the highest frequency of iSNVs was found in ORF8 (1.02 iSNVs/kb), followed by the N gene (0.906 iSNVs/kb) (Figure 1D). These results were consistent with a previous study of SARS-CoV-2 at the SNP level (Zhang et al., 2020). Thus, the imbalance of mutations among genes might occur at the iSNV level and be maintained in the fixation process. In addition, analysis of codon position revealed 2,329, 2,178, and 2,283 iSNVs at the first, second, and third codon positions, respectively (Figure 1E). Fisher's exact test revealed that ORF10 and the E gene had a significantly greater number of iSNVs at the first codon position in comparison with the other codon positions in coordinate genes (Figure 1E).

We next examined the distribution of iSNVs among the individuals. Among the 4,690 iSNV sites, 81.02% were only observed in one individual, and 18.98% were found in at least two individuals, which is comparable with a previous report (Lythgoe et al., 2021). There were 16 highly recurrent iSNVs, which were shared in at least 15 individuals. Among them, 12 sites were found to overlap with high-frequency SNPs (hfSNPs) sites, which had been defined previously in the global SARS-CoV-2 genome database 2019nCoVR, based on more than 5% of individuals (Song et al., 2020; Figure 1F). This phenomenon has also been described in a previous report (Tonkin-Hill et al., 2021) and may be due to convergent positive selection or mutational hotspots. We constructed a simple framework to calculate the distribution of genomic distance between pairs of alleles of iSNVs, and the fitted density line shows

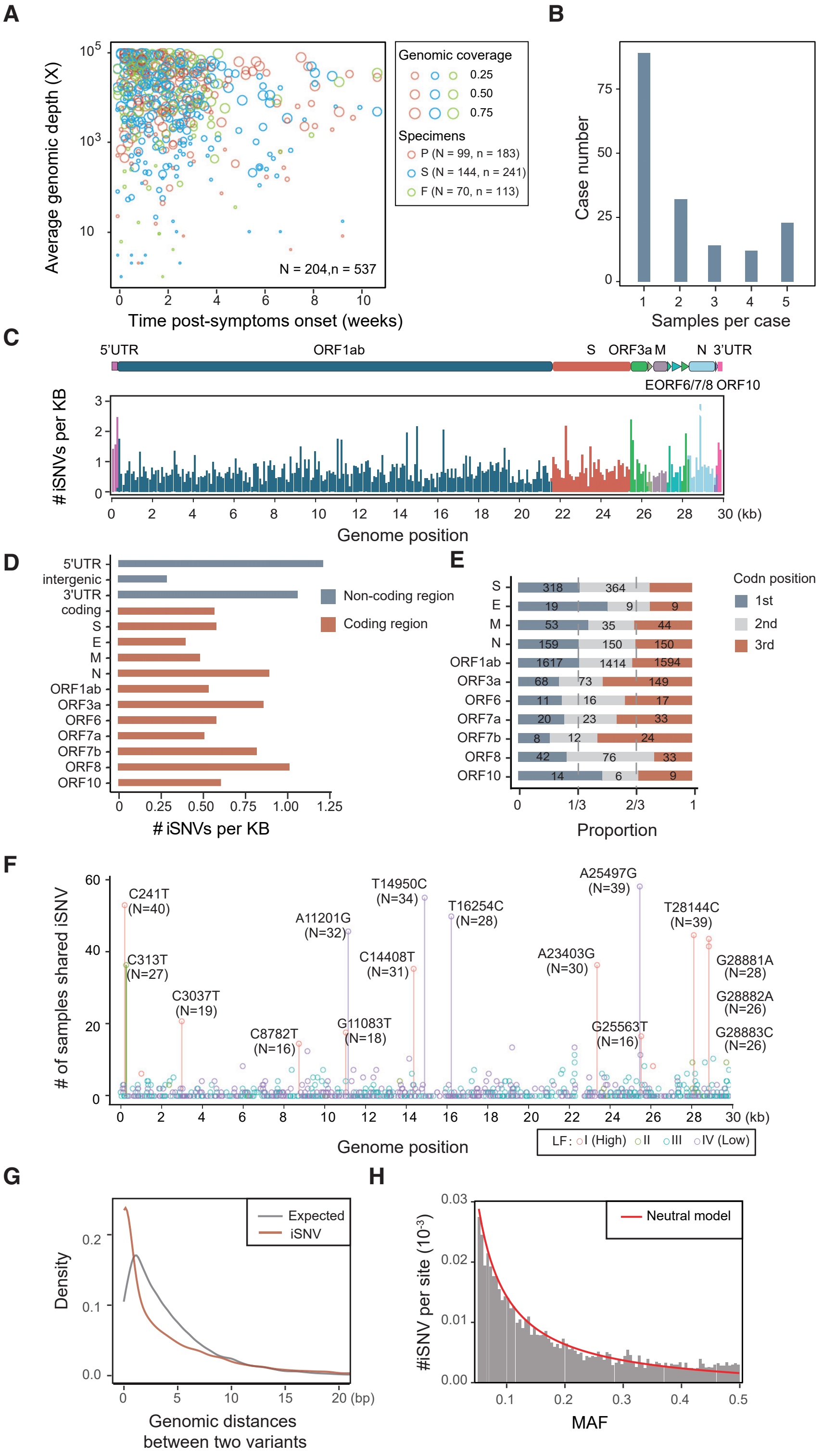

Figure 1. Spatiotemporal analysis of genomic sequencing and iSNV loci identified in this study

(A) Dot plot of the collection time and average sequencing depth of sequenced pharyngeal (red circles), sputum (blue circles), and fecal (green circle) samples.

(B) The accumulative number of cases for single or multiple samples.

(C) Distribution of iSNV frequency in the genome, counted using a window of 100 bp.

(D) Normalized number of iSNVs in coding (red) and non-coding (dark blue) regions.

(E) Proportion of iSNVs occurring in different positions of codons in each gene. The number of iSNVs in each category is marked on the corresponding bar.

(F) Distribution of iSNV loci. The iSNV sites were compared with SNPs reported in the 2019nCoVR database, and sites are marked according to the level of frequency of SNPs occurring in the population (levels I, II, III, and IV colored red, green, blue, and purple, respectively; level I represents the SNPs in public databases with the highest frequencies; STAR Methods). The y axis represents the number of samples, and N represent the number of affected individuals.

(G) Distribution of genomic distances between two variants in expected and identified iSNVs. The red line represents the real data of iSNVs, and the gray line represents the expected curve, which follows the Poisson distribution.

(H) Density of iSNVs against the minor allele frequency. The red line was a fitted line with the generalized linear model and describes how mutations accumulate neutral evolution. The gray histogram represents the real number of definite allele frequency range.

See also Figure S1 and Table S2.

a significant difference compared with the stochastically generated mutations (Figure 1G; Kolmogorov-Smirnov test, $p < 0.001$), suggesting non-stochasticity of iSNV distribution. Moreover, based on a modification of the stochastic birth-death model (Bozic et al., 2016), we predicted allele frequencies to describe how mutations accumulate as cells expand. Although the distribution was similar to the neutral model (Figure 1H), iSNV numbers in the high-frequency alleles were greater than expected values in the neutral evolution model, suggesting potential positive selection of iSNV sites (Figure S1E).

Genetic diversity increases as the disease progresses

To uncover dynamic changes in viral iSNVs in individuals with COVID-19, we performed spatiotemporal analysis of iSNVs along the epidemic period and disease progression using different specimens. First we observed a steady increase in the number of iSNVs over time during the epidemic (estimated value from 0.15 to 0.83 iSNVs/kb within 97 days) (Figure 2A). Similar increases in iSNV numbers were observed in the other viral genomes we

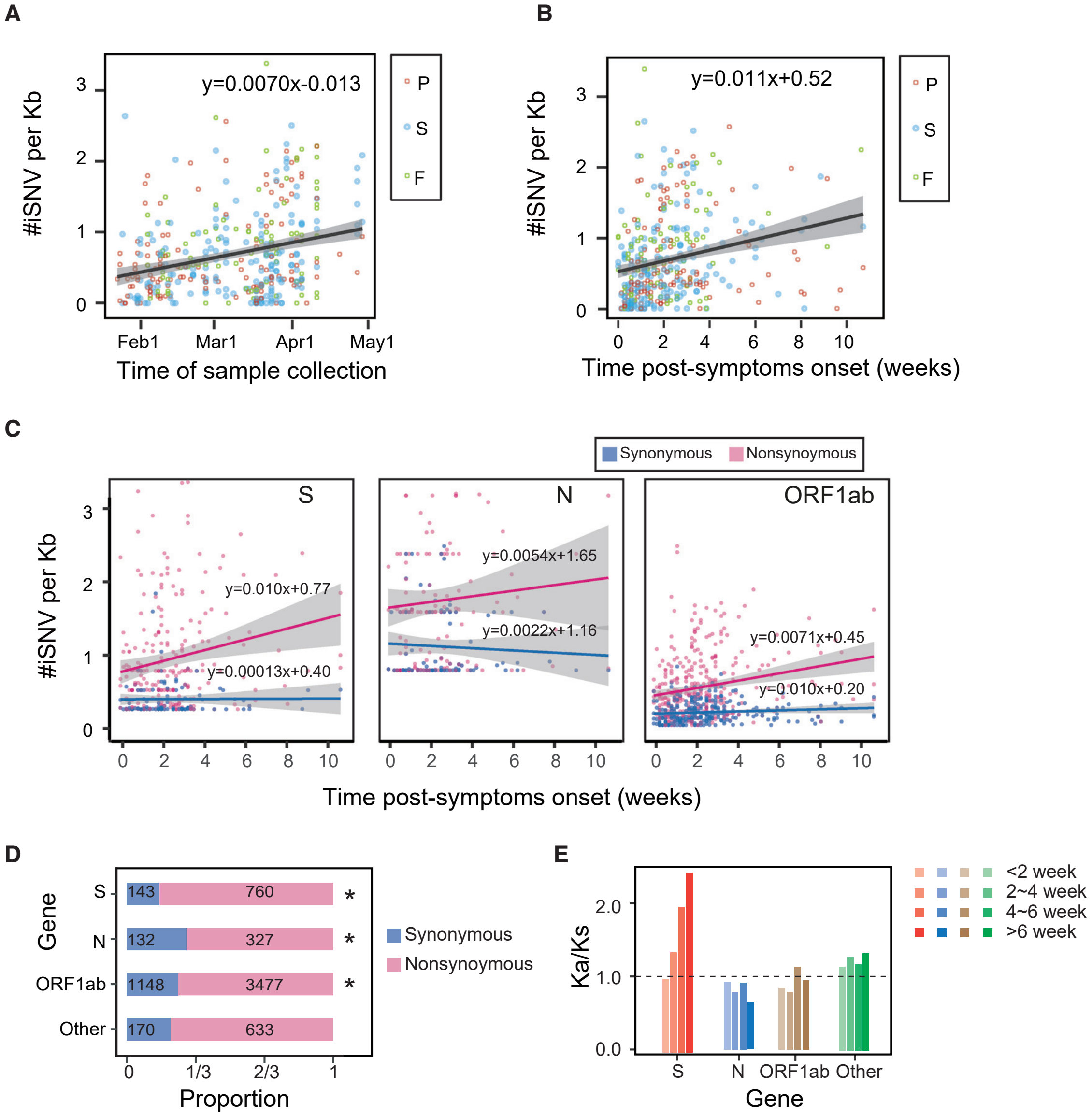

Figure 2. Spatiotemporal analysis of iSNVs reveals increased genetic diversity

(A) Normalized iSNV number against the date of sample collection based on linear regression.

(B) Normalized iSNV number against the time after symptom onset.

(C) Normalized iSNV number causing nonsynonymous and synonymous mutations against time after symptom onset for the S, N, and ORF1ab genes.

(D) Proportion of iSNVs causing nonsynonymous and synonymous mutations in each gene. The number of iSNVs in each category is marked on the corresponding bar. The genes with significantly different numbers of nonsynoymous and synonymous were marked by asterisk ($p < 0.05$, Fisher's exact tes).

(E) Ka/Ks ratio of the S, N, Orf1ab, and other genes in different symptom onset periods.

See also Figure S2.

examined that cause acute and chronic infection (yellow fever virus [YFV], Zika Virus [ZIKV], human immunodeficiency virus [HIV], and hepatitis C virus [HCV]) (Chen et al., 2018; Oliveira et al., 2018; Barton et al., 2016; Skums et al., 2015). Additionally, iSNVs also accumulated during the infection in individual hosts, from 0.52 iSNVs/kb on day 1 to 0.85 iSNVs/kb 30 days after symptom onset (Figure 2B; Table S3). The accumulation was still detectable even after normalization with viral RNA cycle threshold (Ct) values.

However, spatial analysis of the three types of samples, representing different body sites/locations, showed increased genetic diversity in all three specimens along disease progression (Figure S2A). We identified more iSNVs on the initial day and a lower accumulation rate along the disease process in fecal samples compared with those of pharyngeal swab and sputum samples (Figure S2A; p = 0.006, ANOVA).

Positive selection process for iSNVs

To test whether the observed accumulation of genetic diversity was caused by fitness selection, we explored the dynamic change of nonsynonymous and synonymous mutations with disease progression in the S, N, ORF1ab, and other genes. In comparison with neutral synonymous mutations, accumulation of mutations in nonsynonymous regions was more rapid in all genes, and the *S* gene displayed the highest accumulation rate (Figure 2C). Along the genome, we found that 5,197 iSNVs were nonsynonymous mutations, whereas only 1,593 iSNVs were synonymous mutations. The ratio of nonsynonymous to synonymous variants in all individuals was 3.26 (mean ratio of 3.16 observed per individual). The ratio of nonsynonymous to synonymous iSNVs diverges between genes; the ratio in the S gene (ratio = 5.31) was significantly higher than that of the other parts of the viral genome (Figure 2D, $p < 0.001$, Fisher's exact test). The mean values of the minor allele frequencies of nonsynonymous and synonymous iSNVs were 0.189 and 0.195, respectively (Figure S2B). With a simple substitution model, we used the ratio of Ka/Ks, the number of nonsynonymous substitutions per nonsynonymous site (Ka) to the number of synonymous substitutions per synonymous site (Ks), to measure whether the genes in the SARS-CoV-2 genome were under selection pressure. The ratio of Ka/Ks in the S gene increased from 1.01 to 2.46 as the disease progressed, indicating that positive selection occurred with disease progression, at least for the S gene (Figure 2E).

In addition, we use two data sets from the Immune Epitope Database (IEDB) (Dhanda et al., 2019) (experimentally confirmed and predicted epitope regions) (Shrock et al., 2020) to evaluate the fraction of nonsynonymous/synonymous mutations within and outside of epitope regions. The fraction of nonsynonymous mutations in the epitope regions was significantly higher than expected (27.57% versus 25.74%, p = 0.016, Fisher's exact test; Figure S2C). Accordingly, nonsynonymous mutations outside of epitope regions were significantly less frequent (Figure S2C). Further correlation analysis between the fraction of nonsynonymous sites in predicted epitope regions and the time of symptom onset revealed that the number of nonsynonymous sites in the S gene increased as the disease progressed (Figure S2D).

Last, we investigated the dynamics of intra-host evolution in 268 samples from 61 longitudinally sampled individuals. The interval durations between the first and last samples collected were more than 5 days. None of the individuals were subjected to antibody or immunosuppressant treatment. Although the mutation patterns over time varied across individuals, most individuals (45 of 61) showed increased mutational diversity (Figure S2E). We estimated the accumulation rate for each individual using a linear model of iSNV number and post-symptom onset time. Consistent with rapidly accumulated iSNVs in nonsynonymous sites, 84.44% of the individuals (38 of 45) displayed higher accumulation rates in nonsynonymous sites than synonymous sites (Figure S2F). A small number of stable iSNV sites (81 of 3,629) appeared recurrently across time points. In addition, we identified 255 recurrent iSNVs at different time points. Among them, 143 iSNVs showed increased allele frequencies, and the remaining 112 iSNVs had decreased allele frequencies at the latter time points (Figure S2G), providing stronger evidence of potential positive selection within the host.

RNA editing in regions of increased genetic diversity

RNA-editing enzymes can mutagenize single-stranded RNA and DNA molecules and provide a defense mechanism against viruses. Two families of RNA-editing enzymes have been demonstrated to contribute to the mutational spectrum of SARS-CoV-2 (Di Giorgio et al., 2020). The apolipoprotein B mRNA-editing catalytic polypeptide-like deaminase (APOBEC) deaminates cytosines into uracils (C to U, including C to U and G to A), whereas the (RNA-specific adenosine deaminase (ADAR) deaminates adenines into inosines (A to I, including A to G and U to C) (Di Giorgio et al., 2020).

We measured all mutational types for all iSNVs, and the top five iSNV mutation types were ranked as follows (most to least common): U to C, C to U, G to U, A to G, and G to A (Figure 3A); four of them might be introduced by APOBEC and ADAR. Unlike the A-to-I RNA editing signal in the human transcriptome, we did not observe obvious depletion of G bases in position −1 (Figure S3A). To evaluate the dynamic change of RNA editing levels along with disease progress, we calculated the correlations between the minor allele frequencies of iSNVs and the time after symptom onset. The minor allele frequencies of C-to-U and G-to-A mutations because of APOBEC-mediated RNA editing were increased slightly *in vivo*. In contrast, the frequencies of other mutational types, including ADAR-mediated RNA editing *in vivo*, did not increase with the duration of infection. This identification was consistent with previous studies that found that coronavirus infection induced APOBEC activity but not ADAR activity. We next compared the mutational types and their levels of accumulation for nonsynonymous and synonymous mutations. All four substitutions mediated by APOBECs/ADARs were more abundant in nonsynonymous mutations (Figure S3B). In addition, synonymous mutations accumulated more rapidly in comparison with nonsynonymous mutations (Figure 3B). These results suggested that RNA editing mediated by APOBECs was also affected by SARS-CoV-2 infection, especially the rates of C-to-U and G-to-A mutations.

Influence of possible host effects on genetic diversity

An exacerbated inflammatory response has been observed in severe and critical individuals (Hadjadj et al., 2020), and different patterns of immunity have been reported in those of different gender (Takahashi et al., 2020) and age (Zheng et al., 2020) groups. Therefore, we evaluated the influence of host effects on viral mutation and measured dynamic changes in the number of iSNVs within groups of individuals based on gender, age, illness severity, and viral shedding time (Table 1). Each sample was recalibrated based on symptom onset date. Increased genetic diversity of iSNVs was observed in all groups (Figure 4A), suggesting that accumulation of iSNVs occurred in all populations rather than in a specific population. We also observed different slopes and initial values in the fitness linear model between iSNV number and time after symptom onset in these groups (Figure 4B). A higher accumulation rate was observed

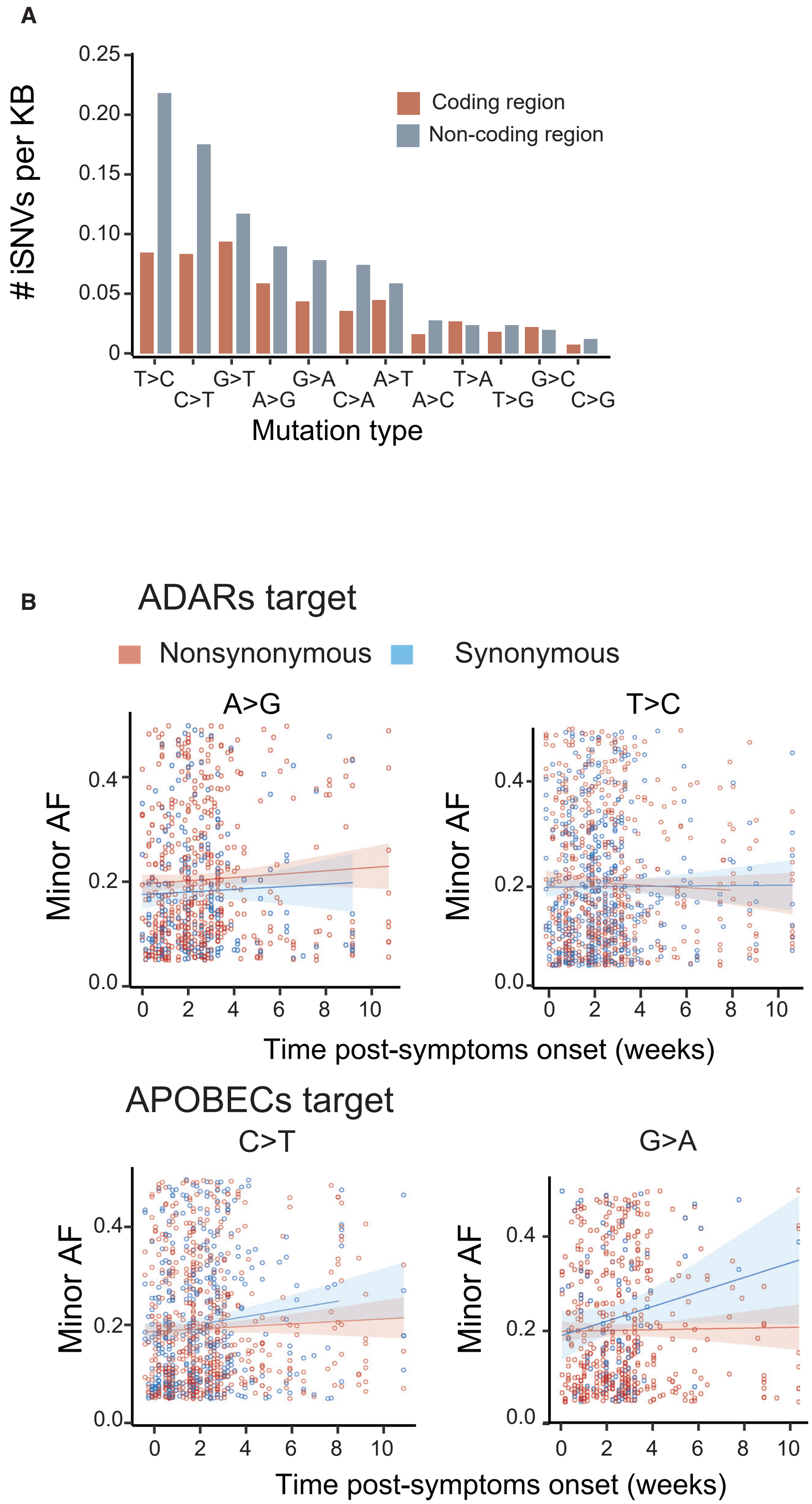

Figure 3. iSNV distributions of different mutation types

(A) Normalized iSNV number for different mutation types. Mutations in coding (red) and non-coding (blue) regions are distinguished by color.

(B) Minor allele frequency (AF) values of ADAR targets (A to I, causing A to G and T to C) and APOBEC targets (C to U, causing C to T and G to A) against time after symptom onset of individuals.

See also Figure S3.

Table 1. Differences in iSNV count, normalized iSNV number, and number of individuals with iSNVs among subpopulations

Characteristics	No. of included individuals (%)	Median iSNV count (qu1–qu3)	Wilcoxon test p value	Median normalized iSNVs (qu1–qu3)	Wilcoxon test p value	Individuals with iSNVs (%)	Fisher's exact test p value
Total	170					163 (95.88%)	
Age groups (years)							
0–15	17 (10.00%)	28 (6–52)	0.648	0.637 (0.339–1.130)	0.243	17 (100%)	1
16–65	131 (77.06%)	17 (5.5–50)	–	0.552 (0.268–0.863)	–	124 (94.65%)	–
>66	22 (12.94%)	37.5 (8.75–63.5)	0.224	0.505 (0.332–0.654)	0.866	22 (100%)	0.594
Gender							
Female	83 (48.82%)	15 (3.5–51)	0.029*	0.478 (0.247–0.795)	0.019*	78 (93.97%)	0.269
Male	87 (51.18%)	25 (9–55.5)		0.599 (0.342–0.962)		85 (97.70%)	
Disease level							
Mild	39 (22.94%)	21 (5.5–57)	0.706	0.489 (0.269–0.812)	0.746	37 (94.87%)	1
Moderate	98 (57.65%)	17.5 (5–44)	–	0.567 (0.270–0.872)	–	93 (94.90%)	–
Severe	33 (19.41%)	21 (11–66)	0.135	0.545 (0.356–0.932)	0.519	33 (100%)	0.330
Infection duration							
0–14	22 (12.94%)	7 (3–18.25)	0.004*	0.338 (0.182–0.576)	0.087	22 (100%)	0.556
15–28	48 (28.23%)	16 (6–43.25)	0.225	0.546 (0.336–0.871)	0.921	46 (95.83%)	1
29–42	43 (25.29%)	29 (12–90)	0.384	0.592 (0.335–0.893)	0.767	41 (95.35%)	1
>43	57 (33.53%)	25 (6–68)	–	0.606 (0.245–0.874)	–	54 (94.74%)	–

See also Table S1 and Table S3. The asterisks represent the p values that were <0.05.

in middle-aged individuals (15–65 year) compared with the elderly (p = 0.037, ANOVA), especially in those whose viral shedding time was more than 6 weeks (p = 0.041, ANOVA; Figure S4A). We also observed a significant increase in nonsynonymous sites in middle-aged compare with elderly individuals (p = 0.035, ANOVA test), whereas the synonymous accumulation rate did not differ among different age groups (Figures S4B and S4C). The different iSNV accumulation rate suggests the presence of a different fitness selection process during the initial infection stage and subsequent infection stages after symptom onset (Figure 4A).

To further investigate specific mutations that could be influenced by host effects, we compared the proportions of individuals with and without recurrently mutated sites (Figure 4C). We constructed a matrix of individuals with or without iSNVs based on 52 iSNV sites shared by more than six individuals among a group of 170. These individuals were categorized into four independent classes: gender, age, illness severity, and viral shedding time (Table 1). Each iSNV site was subjected to an independent Fisher's exact test. Individuals with severe disease, the elderly, those with long viral shedding time, and males preferentially showed significant enrichment in 4, 5, 4, and 8 iSNVs, respectively, compared with individuals with mild/moderate disease, children/middle-aged individuals, those with a short viral shedding time (<6 weeks), and females (Figure 4C). These iSNVs were distributed in ORF1ab, S, N, ORF6, and ORF8. Among the 52 recurrent iSNV sites, we identified 27 sites that preferentially occurred in individuals with severe disease, of which 12 overlapped with previously reported hfSNP sites in the public database 2019nCoVR. In contrast, the 25 iSNVs that preferentially occurred in individuals with moderate disease did not overlap with hfSNPs sites (Figure 4D; $p < 0.001$, Fisher's exact test). This enrichment of hfSNPs sites was not observed in any other categories that were stratified based on gender, age, and viral shedding time, indicating a non-stochastic process.

Uneven purifying selection processes from iSNVs to SNPs

To identify the mutations fixed from iSNVs to SNPs, we compared the genomic sites of iSNVs and SNPs in the 2019nCoVR database (Song et al., 2020; Zhao et al., 2020a). Among 7,037 iSNVs, 15.59% of iSNVs had already been identified as SNPs before our observation period (May 2020), and 11.28% of iSNVs were fixed from May 2020 to December 2020, whereas the remaining iSNVs (73.13%) were not fixed as SNPs (Figure 5A). Nonsynonymous iSNVs displayed a lower fixation rate in comparison with that of synonymous iSNVs (20.92% versus 41.12%, $p < 0.001$, Fisher's exact test; Figure 5B). This finding is supported by a model in which nonsynonymous iSNVs occur at a high frequency in an individual because of positive selection or incomplete purifying selection but are less likely to become fixed in the population because of purifying selection. Next we performed Fisher's exact test to compare the proportion of fixed mutations in each gene, and S and ORF1ab were found to have significantly lower fixation rates (21.04% and 20.56%, $p = 0.005$ and $p < 0.001$, Fisher's exact test, respectively; Figure 5C) at nonsynonymous and synonymous sites (Figure S5A). The nonsynonymous-to-synonymous ratios of iSNVs in ORF1ab, N, and S (excluding D614G) were greater than those estimated for the identified SNPs, consistent with uneven purifying selection of these genes (Figure 5D). With disease progression, iSNV fixation rates in nonsynonymous and synonymous sites were stable in the population (Figures 5E and S5B), indicating a process of similar purifying selection as the

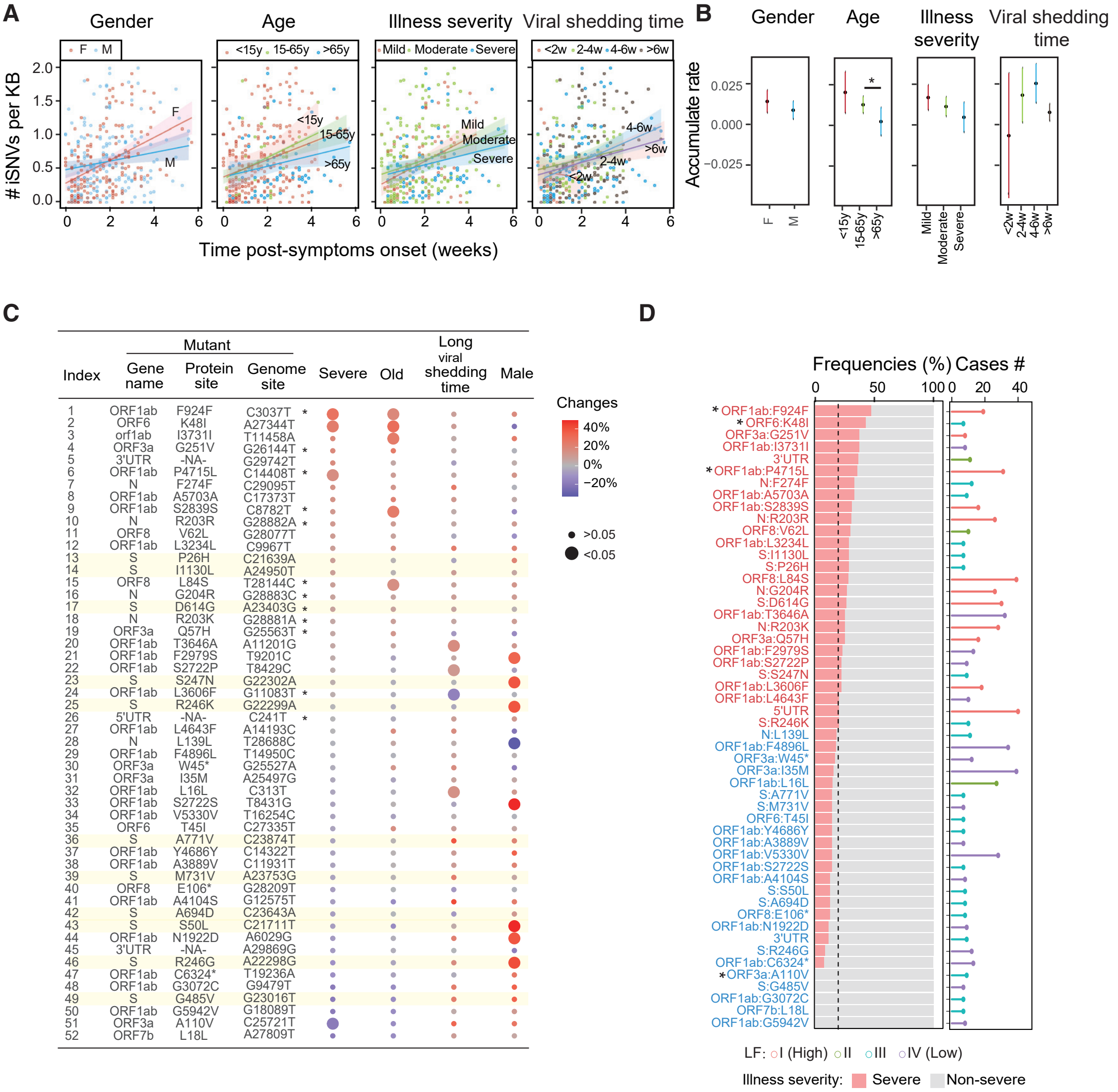

Figure 4. Distribution of iSNVs among different groups of patients

(A) Correlation between normalized iSNV number and onset time for individuals grouped by gender, age, illness severity, and viral shedding time.

(B) The estimated accumulation rate by linear model in (A). The error bar represents the 95% confidence interval of the estimate value.

(C) Effects of gender, age, illness severity, and viral shedding time on iSNV frequency in the population. The size of a point represents the p value of a Fisher's exact test comparing the individuals in each population for each protein site. An asterisk in the genome site represents hfSNPs.

(D) Histogram (left) showing the frequencies of iSNVs related to illness severity. The iSNVs marked with stars are significantly differentially distributed between severe and non-severe populations. Mutations are distinguished by color (red, more severe individuals, gray, less severe individuals). The dashed line represents the average proportion of severe individuals. The variants that signicantly enriched in severe or non-severe population were marked with asterisk ($p < 0.05$, Fisher's exact test). The plot on the right represents the number of cases with these iSNVs. The frequencies of these iSNVs in the public database 2019nCoVR are marked with differently colored lines (levels I, II, III, and IV in red, green, blue, and purple, respectively).

See also Figure S4.

disease progressed. We also observed that mutation might have occurred in iSNVs before they were fixed as SNPs. For example, accumulation of C7051T alleles was observed in our study before May 2020, whereas the first C7051T SNP was not reported until June 2020 (Figure 5F). Although sampling bias might have also limited our observation of SNPs in the early stages of the epidemic period, our observation of mutations at the iSNV level might have increased our detection sensitivity for mutations before they were fixed. These results indicate that iSNVs are a complementary resource of genetic information to illuminate the evolutionary history of SARS-CoV-2.

Molecular functions of S protein variations before purifying selection

The S protein drives cellular binding and entry through receptors and acts as a major determinant of the host range, cell type,

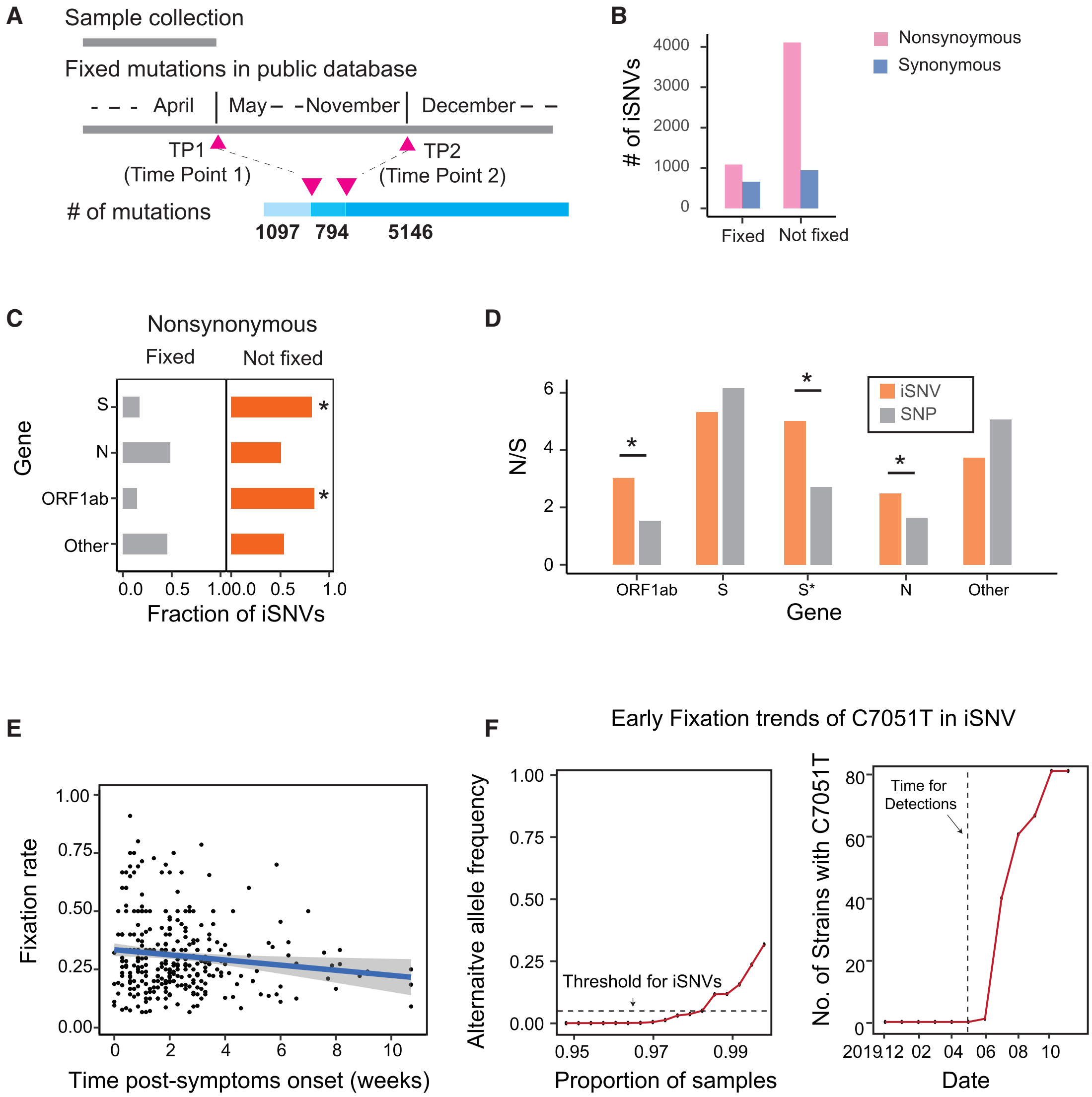

Figure 5. Biased fixation of iSNVs in public SNP databases and local SNP datasets

(A) Number of fixed iSNVs in different time periods.

(B) Number of fixed nonsynonymous and synonymous iSNVs in fixed and unfixed phases.

(C) Fraction of fixed and unfixed nonsynonymous mutations in each gene. The genes with significantly lower fixatation rate were marked with asterisk ($p < 0.05$, Fisher's exact test).

(D) Nonsynonymous/synonymous (N/S) ratio of identified iSNVs and SNPs in each gene. S* represents S genes without the D614G mutation. The asterisks represent the genes with a significant higher N/S ratio of iSNVs compare to SNPs with Fisher's exact test.

(E) Fixation rate of iSNVs over time after symptom onset.

(F) Example of early fixation trends of C7051T in iSNVs in our dataset (left) and in public databases (right).

See also Figure S5.

tissue tropism, and pathogenesis of coronaviruses (Li, 2013). Therefore, we analyzed 21 nonsynonymous sites of 606 iSNV sites identified in the coding region of the S protein, which caused 20 amino acids changes: nine were detected outside of the receptor-binding domain (RBD) region in more than six individuals, including substitution of two amino acids changes in three linked iSNVs (R246E and S247N, caused by A22298G, G22299A, and G22302A; Figure 6A), and 11 resided within the RBD or S1/S2 cleavage sites in more than two individuals, including seven iSNVs located in the receptor-binding motif (RBM). Because few of these mutations had been reported in SARS-CoV-2, we compared the mutation sites of seven iSNVs in the RBM of SARS-CoV-2 with the consensus sequences of SARS-CoV-2-like coronaviruses in other animals (bats and pangolins) to explore their potential molecular functions. All of these sites were heterogeneous, suggesting that mutations in these protein sites may not be random mutations (Figure 6A). In addition, individuals with these mutations had no contact history,

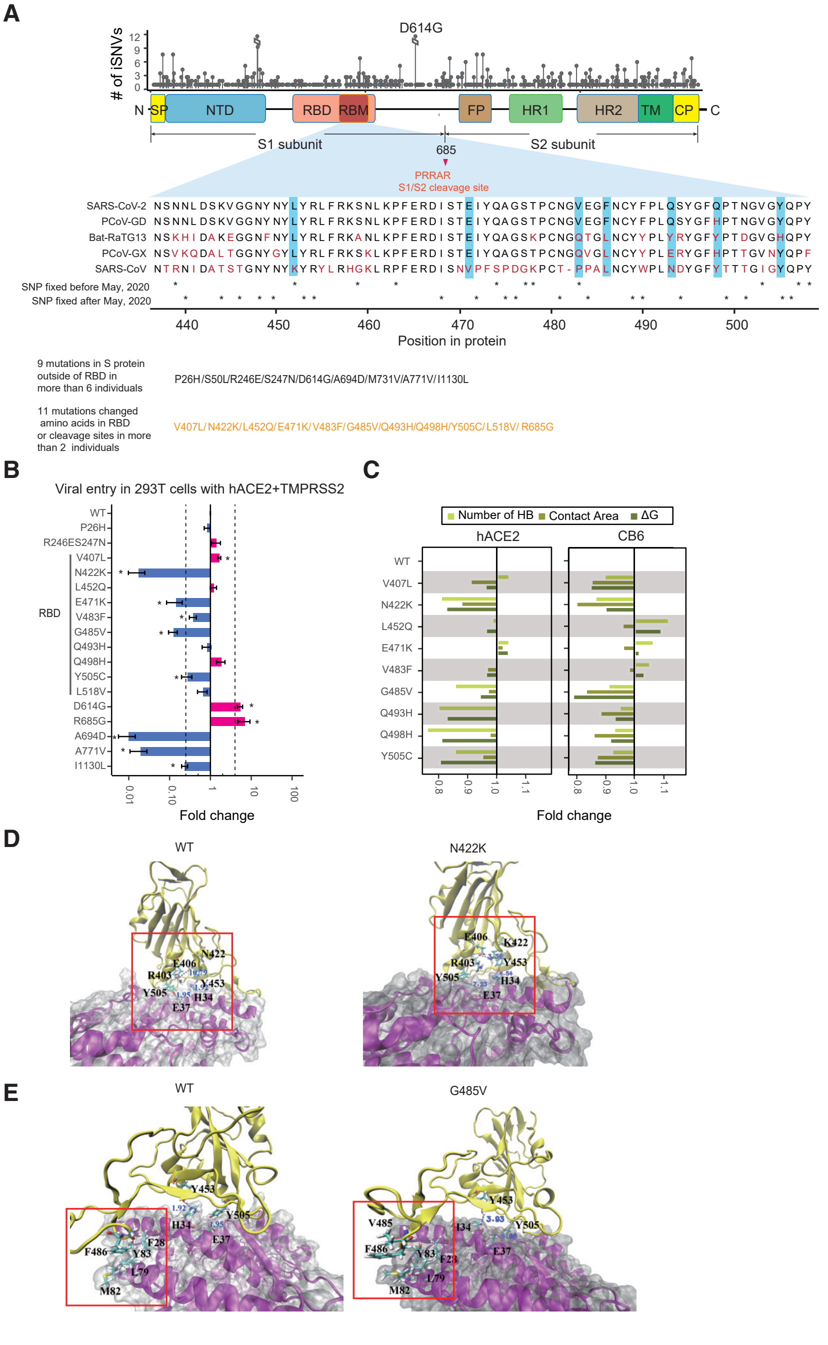

Figure 6. Genetic and molecular structure analysis of iSNVs observed in S protein genes

(A) Location of iSNVs (top) and number of samples with iSNVs. RBD and RBM regions are marked. Shown below are the mutations of amino acid residues in SARS-CoV-2, pangolin CoV isolate MP789 (PCoV-GD), bat-RaTG13, pangolin CoV isolate GX-PL4 (PCoV-GX), and SARS-CoV at locations corresponding to the shared iSNVs in the RBM region. SNPs present in public databases are marked by stars. The GenBank accessions codes for these CoVs are as follows: SARS-CoV-2 (isolate Wuhan-Hu-1, NC_045512.2), SARS-CoV (isolate Tor2, NC_004718.3), bat-RaTG13 (MN996532.1), PCoV-GX (isolate P4L, MT040333.1), and PCoV-GD (isolate MP789, MT084071.1).

(B) Fold change of viral entry in T Rex 293 hACE2 cells for different iSNV mutations. The dashed lines represent fold changes of 0.25 and 4. An asterisk indicates mutants with significantly altered viral entry efficacy based on t tests. Data are represented as mean ± SD. The results were confirmed in at least three separate experiments.

(C) Relative fold change in the number of hydrogen bonds, contact area, and binding energy in molecular dynamics (MD) calculations for mutants compared with WT protein bound to hACE2 and CB6.

(D) Crystal structures of the SARS-CoV-2 RBD/hACE2 complex for WT and N422K mutant proteins. The red square highlights the affected regions.

(E) Crystal structures of the SARS-CoV-2 RBD/hACE2 complex for WT and G485V mutant proteins. The red square highlights the affected regions.

See also Figure S6 and Tables S4, S5, and S6.

except for two individuals with the G485V mutation (Table S4). No iSNVs had emerged in individuals at the first time point of genome sequencing (Figure S6A; Table S4), and no evidence indicated that these iSNVs were linked in the genome. Thus, these results indicate that iSNVs in the RBD seem to be generated by independent viral evolution.

To elucidate the effects of these mutations at the molecular level, we first used a SARS-CoV-2 pseudovirus infection assay in HEK293T cells to assess the viral entry efficacy of 20 of the 22 S protein mutants, excluding S50L and M731V, which we failed to obtain in the mutation assay. Compared with the reference strain, 18 of the 20 tested mutants displayed a decreased (fold change, <0.25; $p < 0.05$, t test) or comparable (fold change, <4 or >0.25) viral entry efficacy; only mutants R685G and D614G exhibited a similar level of increased viral entry efficacy (Figure 6B; Table S5; fold change, >4; $p < 0.05$, t test). Because the L518V mutation is far away from the binding interface between the S protein and hACE2/CB6, and four mutants (N422K, E471K, G485V, and Y505C) displayed a significant decrease (fold change, <0.25) in viral entry efficacy, the other five RBD mutants (V407L, L452Q, V483F, Q493H, and Q498H) were tested for sensitivity to CB6 (Table S6). Wild-type (WT) and D614G viruses were included as controls. Modest differences between these RBD variants and the reference strain (≤4-fold) were observed with regard to susceptibility to CB6 (Table S5). Some variants, including V483F, Q493H, and Q498H, were even more sensitive to CB6 than the reference strain, which indicated that CB6 antibodies could block viral entry despite the RBD mutations.

Next we focused on mutations within the RBM by simulating binding of the corresponding mutants to human angiotensin-converting enzyme 2 (hACE2) (Wang et al., 2020) and CB6 neutralizing antibodies (Shi et al., 2020) using molecular dynamics simulations (Figure 6C). Simulation of the L518V mutation was not conducted for the reasons described above. For comparison, we also simulated binding of the WT RBD to hACE2 and CB6. The Cα root-mean-square deviation (RMSD) values of the complexes of different mutant RBDs bound to hACE2 varied within a range close to the Cα RMSD value of the corresponding complex with the WT RBD, suggesting that the nine mutations did not induce dramatic conformational changes (Figure S6B).

Further exploration of structural characteristics revealed that different mutations affect binding of the RBD to hACE2 in various ways. For example, residue 422 was mutated to change its uncharged N side chain to a positively charged K, producing the N422K mutant. Consequently, a much stronger hydrogen bond (salt bridge) was formed between K422 and E406. In addition, strong repulsion between K422 and R403 as well as attraction between K422 and Y453 caused breakage of the hydrogen bonds between Y505 and E37 as well as those between Y453 and H34. As a result, the number of hydrogen bonds and the contact area formed between the mutant RBDs and hACE2 were reduced (Figure 6D). Regarding the G485V mutation, V has a relatively bulky side chain compared with G; to reposition this bulky side chain, the G485V mutation led to expulsion of F486 from the hydrophobic pocket formed by residues, including F28, L79, M82, and Y83, of hACE2. As a result, the contact area and the number of hydrogen bonds formed between the mutant RBD and hACE2 were reduced. Importantly, the hydrogen bond formed between Y505 of the S protein and E37 of hACE2, which is important for binding, was lost (Figure 6E). As a possible consequence, binding of mutants N422K/G485V to hACE2 was weakened. Binding free energy calculations using the molecular mechanics energies combined with the generalized Born and surface area continuum solvation (MM/GBSA) method also indicated weakened binding of N422K/G485 to hACE2 (Figure 6C).

Changes in hydrogen bonding and contact area were also investigated for other mutants (Figure S6B). Most of the mutants with iSNVs displayed decreased viral entry ability because of fewer hydrogen bonds and/or reduced contact area between mutant RBDs and hACE2. We also analyzed simulation results for complexes between mutant RBDs and the CB6 antibody (Figure S6C). Most of the mutants exhibited a greatly reduced contact area compared with that of the WT sequence. Decreased binding affinity was observed because of fewer hydrogen bonds, consistent with greater binding free energy in the MM/GBSA calculations. Therefore, the observation of mutations in the pseudoviral infection assays and computation of their interaction energies indicated weakened viral infection for most iSNVs identified in the S protein.

DISCUSSION

The ongoing SARS-CoV-2 pandemic is of worldwide concern. SARS-CoV-2 mutations arise naturally as the virus replicates, and the resulting SNPs may affect selection and transmission. Within a year of confirmation of the first case of COVID-19, thousands of mutations involving SNPs had been identified, among which only a very small minority caused changes in SARS-CoV-2 infectivity and immune evasion. Mutations in the SARS-CoV-2 genome can be used to explore signs of selection that accumulate during viral evolution (Sanjuan and Domingo-Calap, 2016; Xue and Bloom, 2020). In the present study, we demonstrated that intra-host variation in SARS-CoV-2 in a set of more than 400 clinical samples was not distributed randomly throughout the genome, suggesting a role of selection. Compared with synonymous mutations, non-synonymous mutations were overrepresented in iSNVs but underrepresented in SNPs (population level). Molecular functional analysis of the effects of mutations in the S protein as well as correlational analysis between mutations and clinical characteristics suggested that mutations increasing disease severity or benefitting immune escape were rare, which could explain the low number of nonsynonymous mutations in populations.

Our sequencing approach provided evidence of two-step fitness selection for intra-host variations in SARS-CoV-2. The first step of selection occurs after randomized mutations are generated, and positive selection (e.g. individual-derived fitness selection) mediates accumulation of nonsynonymous iSNVs, indicating that genetic diversity increases with progression of COVID-19. Positive selection results in two characteristics of iSNVs. The first is an increase in genetic diversity with COVID-19 progression. RNA editing and host immunity may affect this process. Our results show that the rate of iSNV accumulation is significantly higher in middle-aged individuals than in the elderly. Evidence exists that elderly people are under higher immune pressure (Zheng et al., 2020), which may be associated with the accumulation rate of iSNVs. The second characteristic is an uneven distribution of iSNVs among individuals and genomes. The recurrent iSNVs in distinct individuals also imply that these sites were under selection pressure, including positive selection and incomplete purifying selection. The tendency of more iSNVs with allele frequency increase in one individual indicates that these sites were under positive selection. Moreover, these mutations accumulate preferentially in nonsynonymous mutation sites, which might affect key features of the virus, including infectivity, virulence, and immunogenicity. Several other studies on other viruses, such as Ebola virus (Ladner et al., 2015), Lassa virus (Andersen et al., 2015), and influenza virus (Illingworth et al., 2014), support the existence of intra-host positive selection. High rates of mutation accumulation over short time periods in SARS-CoV-2 have been reported in previous studies of immunodeficient or immunosuppressed individuals chronically infected with SARS-CoV-2 (Avanzato et al., 2020). In addition, several recent publications on the SARS-CoV-2 genome identified signals of positive selection (Velazquez-Salinas et al., 2020) and conservation within the gene encoding the S protein.

The second step in the selection process is purifying selection, which accounts for the reduction in the number of nonsynonymous mutations in the transition from iSNVs to SNPs. There are three implications of this. (1) Frequency-dependent interactions and clonal interference may act as important forces driving the selection process. (2) Whether the progeny virus can establish productive infection may affect the spreading of mutations in a population (Lythgoe et al., 2021). (3) The transmission bottleneck is the determining factor for productive infection among hosts and between cells in a single individual. Because individuals sampled in Beijing were mostly imported and/or sporadic cases, it was difficult to measure purifying selection from iSNVs to SNPs in the present study. These current findings provide insight into the emergence of mutations worldwide as well as a direction for efforts aimed at controlling the global COVID-19 pandemic.

As nonsynonymous mutations accumulated in individuals, we also observed 760 nonsynonymous mutations in the S protein. Although the *in vitro* experiment and molecular dynamics simulation proved that the viral entry efficacy of high-frequency iSNV mutations tend to be weakened, it remains unclear whether these weakened viruses persist for lengthy periods of time in individuals with long COVID-19 infection. However, mutations in populations are expected under the current situation. Changes in circumstances, such as widespread adoption of antibody therapy, will alter the selection pressure on each mutation (Zhou et al., 2020). Newly emerging mutations, such as N501Y, E484K, and L452R, show their potential immune escape from the pressure of monoclonal antibodies and vaccines (Li et al., 2021; Motozono et al., 2021). Strong selection pressure arising from antibodies and vaccines might lead to rapid remodeling of virus genetics through direct selection or genetic drift. Therefore, more mutations of SARS-CoV-2 will likely be observed as iSNVs, along with the R685G mutation in cleavage sites, which increases viral entry efficiency, at least in some cell types. These mutations may enhance the persistence of SARS-CoV-2 in multiple organs (Plante et al., 2020), although such SNPs have not yet been identified in public databases.

Given the urgency of vaccine development and treatment strategies, it may not be advisable to wait for mutations to be fixed in populations before efforts are undertaken to demonstrate their effects (Thanh Le et al., 2020). Importantly, early knowledge of potential evolution could guide vaccine design (Li et al., 2020; Poh et al., 2020). Associations between emerging mutations and illness severity as well as treatments should be considered carefully. More genomic data at the intra-host level should be gathered to allow investigation of genetic selection at the whole-genome level, including the potential effects on illness severity, clinical outcomes, and the susceptibility of different populations.

Limitation of the study

Our study describes the dynamic change of iSNVs in individuals. However, because we were limited by the number of individuals, we did not observe a significant difference in distinct groups. The relationship between immune pressure and iSNV dynamics will be an interesting and important future study.

STAR★METHODS

Detailed methods are provided in the online version of this paper and include the following:

SUPPLEMENTAL INFORMATION

Supplemental information can be found online at https://doi.org/10.1016/j.celrep.2021.110205.

ACKNOWLEDGMENTS

We thank all health care workers involved in diagnosis and treatment of individuals with COVID-19 at Beijing Ditan Hospital, Capital Medical University, Qihui Wang for providing the antibody, as well as the BGI for their support. This research was supported by the Beijing Hospital Authority (DFL20191801), the Beijing Municipal Science & Technology Commission (Z201100007920017 and Z201100005420012), and the National Natural Science Foundation of China (92053202, 22050003, and 21873007).

AUTHOR CONTRIBUTIONS

Jiarui Li, P.D., and N.D. performed sequencing data analyses. D.C. and X.Z. performed pseudoviral assay infection experiments. L.Y. and Y.Q.G. performed molecular dynamics analyses. F.Z., J.Z., Y.S., R.S., W.X., Z.C., X.W., Jingyuan Liu, Y.X., G.G., Q.W., L.P., and F.Y. collected and analyzed clinical data. C.S., K.H., L.D., Jie Li, J.Y., M.H., J.H., and Y.Y. performed most of the experiments. A.W., Y.Q.G., Y.H., J.W., and G.G. provided intellectual input and helped to interpret the data. Jiarui Li, P.D., L.Y., D.C., C.C., Y.Q.G., and H.Z. wrote the manuscript. All authors discussed the results and commented on the manuscript. C.C., H.Z., J.W., Y.H., Y.Q.G., and G.G. supervised the study.

DECLARATION OF INTERESTS

The authors declare no competing interests.

Received: June 8, 2021
Revised: October 10, 2021
Accepted: December 13, 2021
Published: January 11, 2022

REFERENCES

Andersen, K.G., Shapiro, B.J., Matranga, C.B., Sealfon, R., Lin, A.E., Moses, L.M., Folarin, O.A., Goba, A., Odia, I., Ehiane, P.E., et al. (2015). Clinical sequencing uncovers origins and evolution of Lassa virus. Cell *162*, 738–750.

Avanzato, V.A., Matson, M.J., Seifert, S.N., Pryce, R., Williamson, B.N., Anzick, S.L., Barbian, K., Judson, S.D., Fischer, E.R., Martens, C., et al. (2020). Case study: prolonged infectious SARS-CoV-2 shedding from an asymptomatic immunocompromised individual with cancer. Cell *183*, 1901–1912. e9.

Barton, J.P., Goonetilleke, N., Butler, T.C., Walker, B.D., McMichael, A.J., and Chakraborty, A.K. (2016). Relative rate and location of intra-host HIV evolution to evade cellular immunity are predictable. Nat. Commun. *7*, 11660.

Beauchemin, C.A., and Handel, A. (2011). A review of mathematical models of influenza a infections within a host or cell culture: lessons learned and challenges ahead. BMC Public Health *11*, S7.

Bozic, I., Gerold, J.M., and Nowak, M.A. (2016). Quantifying clonal and subclonal passenger mutations in cancer evolution. PLoS Comput. Biol. *12*, e1004731.

Chan, J.F., Yuan, S., Kok, K.H., To, K.K., Chu, H., Yang, J., Xing, F., Liu, J., Yip, C.C., Poon, R.W., et al. (2020). A familial cluster of pneumonia associated with the 2019 novel coronavirus indicating person-to-person transmission: a study of a family cluster. Lancet *395*, 514–523.

Chen, C., Jiang, D., Ni, M., Li, J., Chen, Z., Liu, J., Ye, H., Wong, G., Li, W., Zhang, Y., et al. (2018). Phylogenomic analysis unravels evolution of yellow fever virus within hosts. PLoS Negl. Trop. Dis. *12*, e0006738.

Chen, C., Li, J., Di, L., Jing, Q., Du, P., Song, C., Li, J., Li, Q., Cao, Y., Xie, X.S., et al. (2020). MINERVA: A facile strategy for SARS-CoV-2 whole-genome deep sequencing of clinical samples. Mol. Cell *80*, 1123–1134.e4.

Coronaviridae Study Group of the International Committee on Taxonomy of, V (2020). The species severe acute respiratory syndrome-related coronavirus: classifying 2019-nCoV and naming it SARS-CoV-2. Nat. Microbiol. *5*, 536–544.

Darden, T., York, D., and Pedersen, L. (1993). Particle mesh Ewald: an N• log (N) method for Ewald sums in large systems. The Journal of chemical physics *98*, 10089–10092.

Debbink, K., McCrone, J.T., Petrie, J.G., Truscon, R., Johnson, E., Mantlo, E.K., Monto, A.S., and Lauring, A.S. (2017). Vaccination has minimal impact on the intrahost diversity of H3N2 influenza viruses. PLoS Pathog. *13*, e1006194.

Dhanda, S.K., Mahajan, S., Paul, S., Yan, Z., Kim, H., Jespersen, M.C., Jurtz, V., Andreatta, M., Greenbaum, J.A., Marcatili, P., et al. (2019). IEDB-AR: immune epitope database-analysis resource in 2019. Nucleic Acids Res. *47*, W502–W506.

Di Giorgio, S., Martignano, F., Torcia, M.G., Mattiuz, G., and Conticello, S.G. (2020). Evidence for host-dependent RNA editing in the transcriptome of SARS-CoV-2. Sci. Adv. *6*, eabb5813.

Forni, D., Cagliani, R., Mozzi, A., Pozzoli, U., Al-Daghri, N., Clerici, M., and Sironi, M. (2016). Extensive positive selection drives the evolution of nonstructural proteins in lineage C betacoronaviruses. J. Virol. *90*, 3627–3639.

Gao, S.J., Guo, H., and Luo, G. (2021). Omicron variant (B.1.1.529) of SARS-CoV-2, a global urgent public health alert. J. Med. Virol. https://doi.org/10.1002/jmv.27491.

Gudbjartsson, D.F., Helgason, A., Jonsson, H., Magnusson, O.T., Melsted, P., Norddahl, G.L., Saemundsdottir, J., Sigurdsson, A., Sulem, P., and Agustsdottir, A.B. (2020). Spread of SARS-CoV-2 in the Icelandic population. N. Engl. J. Med. *11*, 2302–2315.

Hadjadj, J., Yatim, N., Barnabei, L., Corneau, A., Boussier, J., Smith, N., Pere, H., Charbit, B., Bondet, V., Chenevier-Gobeaux, C., et al. (2020). Impaired type I interferon activity and inflammatory responses in severe COVID-19 patients. Science *369*, 718–724.

Holmes, E.C., Dudas, G., Rambaut, A., and Andersen, K.G. (2016). The evolution of Ebola virus: Insights from the 2013-2016 epidemic. Nature *538*, 193–200.

Illingworth, C.J., Fischer, A., and Mustonen, V. (2014). Identifying selection in the within-host evolution of influenza using viral sequence data. PLoS Comput. Biol. *10*, e1003755.

Jhun, H., Park, H.Y., Hisham, Y., Song, C.S., and Kim, S. (2021). SARS-CoV-2 Delta (B.1.617.2) variant: A unique T478K mutation in receptor binding motif (RBM) of spike gene. Immune Netw. *21*, e32.

Jorgensen, W.L., Chandrasekhar, J., Madura, J.D., Impey, R.W., and Klein, M.L. (1983). Comparison of simple potential functions for simulating liquid water. J. Chem. Phys. *79*, 926–935.

Korber, B., Fischer, W.M., Gnanakaran, S., Yoon, H., Theiler, J., Abfalterer, W., Hengartner, N., Giorgi, E.E., Bhattacharya, T., Foley, B., et al. (2020). Tracking changes in SARS-CoV-2 spike: Evidence that D614G increases infectivity of the COVID-19 virus. Cell *182*, 812–827.e819.

Ladner, J.T., Wiley, M.R., Mate, S., Dudas, G., Prieto, K., Lovett, S., Nagle, E.R., Beitzel, B., Gilbert, M.L., Fakoli, L., et al. (2015). Evolution and spread of Ebola virus in Liberia, 2014-2015. Cell Host Microbe *18*, 659–669.

Langmead, B., and Salzberg, S.L. (2012). Fast gapped-read alignment with Bowtie 2. Nat. Methods *9*, 357–359.

Li, F. (2013). Receptor recognition and cross-species infections of SARS coronavirus. Antivir. Res. *100*, 246–254.

Li, H., Handsaker, B., Wysoker, A., Fennell, T., Ruan, J., Homer, N., Marth, G., Abecasis, G., Durbin, R., and Genome Project Data Processing, S. (2009). The sequence alignment/map format and SAMtools. Bioinformatics *25*, 2078–2079.

Li, Q., Nie, J., Wu, J., Zhang, L., Ding, R., Wang, H., Zhang, Y., Li, T., Liu, S., Zhang, M., et al. (2021). SARS-CoV-2 501Y.V2 variants lack higher infectivity but do have immune escape. Cell *184*, 2362–2371. e9.

Li, Q., Wu, J., Nie, J., Zhang, L., Hao, H., Liu, S., Zhao, C., Zhang, Q., Liu, H., Nie, L., et al. (2020). The impact of mutations in SARS-CoV-2 spike on viral infectivity and antigenicity. Cell *182*, 1284–1294.e1289.

Lythgoe, K.A., Hall, M., Ferretti, L., de Cesare, M., MacIntyre-Cockett, G., Trebes, A., Andersson, M., Otecko, N., Wise, E.L., Moore, N., et al. (2021). SARS-CoV-2 within-host diversity and transmission. Science *372*, eabg0821.

Maier, J.A., Martinez, C., Kasavajhala, K., Wickstrom, L., Hauser, K.E., Simmerling, C., and computation. (2015). ff14SB: improving the accuracy of protein side chain and backbone parameters from ff99SB. J. Chem. Theory Comput. *11*, 3696–3713.

McCrone, J.T., Woods, R.J., Martin, E.T., Malosh, R.E., Monto, A.S., and Lauring, A.S. (2018). Stochastic processes constrain the within and between host evolution of influenza virus. Elife *7*, e35962.

Motozono, C., Toyoda, M., Zahradnik, J., Saito, A., Nasser, H., Tan, T.S., Ngare, I., Kimura, I., Uriu, K., Kosugi, Y., et al. (2021). SARS-CoV-2 spike L452R variant evades cellular immunity and increases infectivity. Cell Host Microbe *29*, 1124–1136 e1111.

Ni, M., Chen, C., and Liu, D. (2018). An assessment of amplicon-sequencing based method for viral intrahost analysis. Virol. Sin. *33*, 557–560.

Ni, M., Chen, C., Qian, J., Xiao, H.X., Shi, W.F., Luo, Y., Wang, H.Y., Li, Z., Wu, J., Xu, P.S., et al. (2016). Intra-host dynamics of Ebola virus during 2014. Nat. Microbiol. *1*, 16151.

Oliveira, D.B.L., Durigon, G.S., Mendes, E.A., Ladner, J.T., Andreata-Santos, R., Araujo, D.B., Botosso, V.F., Paola, N.D., Neto, D.F.L., Cunha, M.P., et al. (2018). Persistence and intra-host genetic evolution of Zika virus infection in symptomatic adults: A special view in the male reproductive system. Viruses *10*, 615.

Plante, J.A., Liu, Y., Liu, J., Xia, H., Johnson, B.A., Lokugamage, K.G., Zhang, X., Muruato, A.E., Zou, J., Fontes-Garfias, C.R., et al. (2020). Spike mutation D614G alters SARS-CoV-2 fitness. Nature *592*, 116–121.

Poh, C.M., Carissimo, G., Wang, B., Amrun, S.N., Lee, C.Y., Chee, R.S., Fong, S.W., Yeo, N.K., Lee, W.H., Torres-Ruesta, A., et al. (2020). Two linear epitopes on the SARS-CoV-2 spike protein that elicit neutralising antibodies in COVID-19 patients. Nat. Commun. *11*, 2806.

Popa, A., Genger, J.W., Nicholson, M.D., Penz, T., Schmid, D., Aberle, S.W., Agerer, B., Lercher, A., Endler, L., Colaco, H., et al. (2020). Genomic epidemiology of superspreading events in Austria reveals mutational dynamics and transmission properties of SARS-CoV-2. Sci. Transl Med. *12*, eabe2555.

Rambaut, A., Holmes, E.C., O'Toole, A., Hill, V., McCrone, J.T., Ruis, C., du Plessis, L., and Pybus, O.G. (2020). A dynamic nomenclature proposal for SARS-CoV-2 lineages to assist genomic epidemiology. Nat. Microbiol. *5*, 1403–1407.

Ryckaert, J.-P., Ciccotti, G., and Berendsen, H.J. (1977). Numerical integration of the Cartesian equations of motion of a system with constraints: molecular dynamics of n-alkanes. J. Comput. Phys. *23*, 327–341.

Sanjuan, R., and Domingo-Calap, P. (2016). Mechanisms of viral mutation. Cell Mol. Life Sci. *73*, 4433–4448.

Shi, R., Shan, C., Duan, X., Chen, Z., Liu, P., Song, J., Song, T., Bi, X., Han, C., Wu, L., et al. (2020). A human neutralizing antibody targets the receptor-binding site of SARS-CoV-2. Nature *584*, 120–124.

Shrock, E., Fujimura, E., Kula, T., Timms, R.T., Lee, I.H., Leng, Y., Robinson, M.L., Sie, B.M., Li, M.Z., Chen, Y., et al. (2020). Viral epitope profiling of COVID-19 patients reveals cross-reactivity and correlates of severity. Science *370*, eabd4250.

Shu, Y., and McCauley, J. (2017). GISAID: Global initiative on sharing all influenza data - from vision to reality. Euro Surveill. *22*, 30494.

Skums, P., Bunimovich, L., and Khudyakov, Y. (2015). Antigenic cooperation among intrahost HCV variants organized into a complex network of cross-immunoreactivity. Proc. Natl. Acad. Sci. U S A. *112*, 6653–6658.

Song, S., Ma, L., Zou, D., Tian, D., Li, C., Zhu, J., Chen, M., Wang, A., Ma, Y., and Li, M. (2020). The global landscape of SARS-CoV-2 genomes, variants, and haplotypes in 2019nCoVR. Genom. Proteom. Bioinform. *18*, 749–759.

Takahashi, T., Ellingson, M.K., Wong, P., Israelow, B., Lucas, C., Klein, J., Silva, J., Mao, T., Oh, J.E., Tokuyama, M., et al. (2020). Sex differences in immune responses that underlie COVID-19 disease outcomes. Nature *588*, 315–320.

Tang, X., Wu, C., Li, X., Song, Y., Yao, X., Wu, X., Duan, Y., Zhang, H., Wang, Y., Qian, Z., et al. (2020). On the origin and continuing evolution of SARS-CoV-2. Natl. Sci. Rev. *7*, 1012–1023.

Thanh Le, T., Andreadakis, Z., Kumar, A., Gomez Roman, R., Tollefsen, S., Saville, M., and Mayhew, S. (2020). The COVID-19 vaccine development landscape. Nat. Rev. Drug Discov. *19*, 305–306.

Tonkin-Hill, G., Martincorena, I., Amato, R., Lawson, A.R., Gerstung, M., Johnston, I., Jackson, D.K., Park, N., Lensing, S.V., Quail, M.A., et al. (2021). Patterns of within-host genetic diversity in SARS-CoV-2. Elife *10*, e66857.

Velazquez-Salinas, L., Zarate, S., Eberl, S., Gladue, D.P., Novella, I., and Borca, M.V. (2020). Positive selection of ORF1ab, ORF3a, and ORF8 genes drives the early evolutionary trends of SARS-CoV-2 during the 2020 COVID-19 pandemic. Front Microbiol. *11*, 550674.

Wang, D., Zhang, Y., Zhang, Z., Zhu, J., and Yu, J. (2010). KaKs_Calculator 2.0: a toolkit incorporating gamma-series methods and sliding window strategies. Genom. Proteom. Bioinform. *8*, 77–80.

Wang, Q., Zhang, Y., Wu, L., Niu, S., Song, C., Zhang, Z., Lu, G., Qiao, C., Hu, Y., Yuen, K.Y., et al. (2020). Structural and functional basis of SARS-CoV-2 entry by using human ACE2. Cell *181*, 894–904 e899.

Wu, F., Zhao, S., Yu, B., Chen, Y.M., Wang, W., Song, Z.G., Hu, Y., Tao, Z.W., Tian, J.H., Pei, Y.Y., et al. (2020). A new coronavirus associated with human respiratory disease in China. Nature *579*, 265–269.

Xue, K.S., and Bloom, J.D. (2020). Linking influenza virus evolution within and between human hosts. Virus Evol. *6*, veaa010.

Xue, K.S., Moncla, L.H., Bedford, T., and Bloom, J.D. (2018). Within-host evolution of human influenza virus. Trends Microbiol. *26*, 781–793.

Zhang, X., Tan, Y., Ling, Y., Lu, G., Liu, F., Yi, Z., Jia, X., Wu, M., Shi, B., Xu, S., et al. (2020). Viral and host factors related to the clinical outcome of COVID-19. Nature *583*, 437–440.

Zhang, Z., Li, J., and Yu, J. (2006). Computing Ka and Ks with a consideration of unequal transitional substitutions. BMC Evol. Biol. *6*, 44.

Zhao, W.M., Song, S.H., Chen, M.L., Zou, D., Ma, L.N., Ma, Y.K., Li, R.J., Hao, L.L., Li, C.P., Tian, D.M., et al. (2020a). The 2019 novel coronavirus resource. Yi Chuan. *42*, 212–221.

Zhao, X., Chen, D., Szabla, R., Zheng, M., Li, G., Du, P., Zheng, S., Li, X., Song, C., Li, R., et al. (2020b). Broad and differential animal angiotensin-converting enzyme 2 receptor usage by SARS-CoV-2. J. Virol. *94*, e00920–e00940.

Zhao, X., Guo, F., Comunale, M.A., Mehta, A., Sehgal, M., Jain, P., Cuconati, A., Lin, H., Block, T.M., Chang, J., et al. (2015). Inhibition of endoplasmic reticulum-resident glucosidases impairs severe acute respiratory syndrome coronavirus and human coronavirus NL63 spike protein-mediated entry by altering the glycan processing of angiotensin I-converting enzyme 2. Antimicrob. Agents Chemother. *59*, 206–216.

Zheng, Y., Liu, X., Le, W., Xie, L., Li, H., Wen, W., Wang, S., Ma, S., Huang, Z., Ye, J., et al. (2020). A human circulating immune cell landscape in aging and COVID-19. Protein Cell *11*, 740–770.

Zhou, W., Spoto, M., Hardy, R., Guan, C., Fleming, E., Larson, P.J., Brown, J.S., and Oh, J. (2020). Host-specific evolutionary and transmission dynamics shape the functional diversification of *Staphylococcus epidermidis* in human Skin. Cell *180*, 454–470.e418.

Zhu, N., Zhang, D., Wang, W., Li, X., Yang, B., Song, J., Zhao, X., Huang, B., Shi, W., Lu, R., et al. (2020). A novel coronavirus from patients with pneumonia in China, 2019. N. Engl. J. Med. *382*, 727–733.

STAR★METHODS

KEY RESOURCE TABLE

REAGENT or RESOURCE	SOURCE	IDENTIFIER
Antibodies		
CB6	Laboratory of Qihui Wang; Shi et al., 2020	N/A
Bacterial and virus strains		
TransStbl3 Chemically Competent Cell	TransGen Biotech	Cat#CD521-01
Critical commercial assays		
Steady-Glo Luciferase Assay System	Promega	Cat#E1501
Lenti-X p24 Rapid Titer Kit	Clontech	Cat#632200
TargetSeq One Cov Kit (iGeneTech,)	iGeneTech	Cat#502002-V1
Deposited data		
Sequencing data for the SARS-CoV-2 genome	This study	NGDC: HRA000181, HRA000349
Original experimental data	This study	Mendeley Data: https://doi.org/10.17632/rmr4bcsgrp.1
Original code	This study	Zenodo: https://doi.org/10.5281/zenodo.5703845
Experimental models: Cell lines		
HEK-293T	ATCC	Cat#CRL-3216
Flp-In T-Rex Cell Line	Life Technologies	Cat#R780-07
Experimental models: Organisms/strains		
See supplementary data: Table S12		N/A
Software and algorithms		
Bowtie2 v2.1.0	Langmead and Salzberg (2012)	http://bowtie-bio.sourceforge.net/bowtie2/index.shtml
SAMtools v 1.3.1	Li et al. (2009)	http://samtools.sourceforge.net/
iSNV-calling scripts	Ni et al. (2016)	https://github.com/generality/iSNV-calling/
Ka_Ks calculater	Wang et al. (2010), Zhang et al. (2006)	https://sourceforge.net/projects/kakscalculator2/
AMBER FF14SB	Maier et al. (2015)	http://ambermd.org/AmberTools.php

RESOURCE AVAILABILITY

Lead contact

Further information and requests for resources and reagents should be directed to and will be fulfilled by the lead contact, Prof. Chen Chen (chenchen1@ccmu.edu.cn).

Materials availability

This study did not generate new unique reagents.

Data and code availability

- The sequencing data has been submitted to the National Genomics Data Center, China National Center for Bioinformation and are publicly available as of the date of publication. Accession numbers are listed in the key resources table. Original pseudovirus assay and other experimental data have been deposited at Mendeley and are publicly available as of the date of publication.
- The original code is available in Zenodo at https://doi.org/10.5281/zenodo.5703845.
- Any additional information required to reanalyze the data reported in this paper is available from the lead contact upon request.

EXPERIMENTAL MODEL AND SUBJECT DETAILS

Patients and clinical cohort

Our study included all confirmed and admitted patients with at Beijing Ditan Hospital, Beijing, China, where the first case in Beijing was recorded, between January 20 and April 30, 2020. We enrolled 204 cases, accounting for 34.4% of confirmed patients in Beijing, containing 102 female and 102 male, 22 children (<15 y), 226 mid-age (>15y and <65y) and 29 elders (>65y) (Table S1). All patients were confirmed by RT-PCR tests on pharyngeal swab samples at Beijing Ditan Hospital. All patients were treated and managed in the ward after diagnosis. Standardised electronic medical records were employed to collect basic demographic and epidemiological information, medical histories, and clinical data. Patients were diagnosed and discharged according to the 7th Guideline for the Diagnosis and Treatment of COVID-19 from the National Health Commission of the People's Republic of China (https://www.chinadaily.com.cn/pdf/2020/1.Clinical.Protocols.for.the.Diagnosis.and.Treatment.of.COVID-19.V7.pdf). Patients were classified into three severity categories: mild, moderate and severe (traditionally defined as severe and critical illness). Briefly, mild cases were those with mild clinical symptoms, for whom imaging showed no sign of pneumonia. Moderate cases were those showing fever and respiratory symptoms with radiological findings of pneumonia. Severe cases included adult cases meeting any of the following criteria: (1) respiratory distress (R30 breaths/min), (2) oxygen saturation percentage of 93% at rest, (3) arterial partial pressure of oxygen (PaO2)/fraction of inspired oxygen (FiO2) percentage of 300 mmHg.

The internal use of samples for diagnostic workflow optimisation conformed to the medical ethical rules of each of the participating partners and was approved by the Review Board of Beijing Ditan Hospital and the Ethics Committee of the State Key Laboratory of Pathogen and Biosecurity (KT2020-006-01).

EPIDEMIC ANALYSIS

Through detailed epidemiological investigation, we identified 26 infection clusters involving 79 patients (Supplementary Data Table S7). No super-spreader events were identified.

Time point labels for each patient were defined based on clinical characteristics. For patients with symptoms, we set the time of symptoms onset as day 0. For asymptotic patients, day 0 was set as the day of the first positive RT-PCR test. The date of negative transition was defined as the date when all specimens (including pharyngeal swab, sputum and faecal specimens) yielded negative results. Viral shedding time was calculated from day 0 to the date of negative transition.

Samples from the same individual whose samples collected duration between the first and last time points more than 5 days were defined as longitudinal samples. Among the 165 patients whose viral shedding time more than 5 days, we selected 61 patients with longitudinal samples.

METHOD DETAILS

Laboratory procedures

Clinical samples, including pharyngeal swabs, sputum and faecal specimens for RT-PCR tests, were collected in replicate according to the instructions of the infection prevention and control measures in the Chinese guidance on infection prevention and control in healthcare settings. RNA was extracted using previously described methods appropriate for P2+ and/or P3 laboratories (Chan et al., 2020). Viral RNA was extracted using a QIAamp Viral RNA Mini Kit according to the manufacturer's instructions, except that carrier RNA was omitted to facilitate downstream high-throughput sequencing analysis. DNA was removed from the samples via DNase I (NEB) digestion. The resulting total RNA was concentrated using an RNA Clean & Concentrator-5 Kit (Zymo Research), and its quality was assessed by a Fragment Analyzer Automated CE System (AATI). Quantification was performed by Qubit 2.0 (Invitrogen). Diagnostic real-time RT-PCR assays targeting the open reading frame 1ab (ORF1ab) region and nucleoprotein (N) gene of SARS-CoV-2 were performed as described elsewhere (Zhu et al., 2020). A cycle threshold (Ct) value ≤ 37 in at least one gene was interpreted as a positive test for SARS-CoV-2 according to Chinese national guidelines. The Ct values of the tested samples ranged from 12.00 to 37.52.

High-throughput genomic sequencing of the viral genome

We collected 183 pharyngeal swab samples, 241 sputum samples, and 113 faecal samples for meta-transcriptomic sequencing. Viral RNA was extracted using the protocol described above. After performing ribosomal RNA (rRNA) removal using the MGIEasy rRNA Depletion Kit (BGI, Shenzhen, China), we used the novel metagenomic RNA enrichment viral sequencing (MINERVA) approach to obtain virus sequences (Chen et al., 2020). This approach uses direct tagmentation of RNA/cDNA hybrids with Tn5 transposase to greatly simplify the sequencing library construction process, allowing us to conduct rapid library preparation using low volume input RNA templates (5.4 μL) within 4 h. The step-by-step protocol is available in a previous paper (Chen et al., 2020). Briefly, 2.7 mL RNA (after rRNA and DNA removal) was used for standard SHERRY reverse transcription, with the following modifications: (1) 10 pmol random decamers (N10) were added to improve coverage and (2) initial concentrations of dNTPs and oligo-dT (T30VN) were increased to 25 mM and 100 mM, respectively. For the 5.4 mL and 10.8 mL input volumes, the entire reaction was simply scaled up 2- and 4-fold, respectively. The RNA/cDNA hybrid was tagmented in TD reaction buffer (10 mM Tris-HCl pH 7.6, 5 mM $MgCl_2$, 10% DMF) supplemented with 3.4% PEG8000 (VWR Life Science), 1 mM ATP (NEB), and 1 U/mL RNase inhibitor (TaKaRa). The reaction was incubated at 55°C for 30 min. A 20 mL volume of tagmentation product was mixed with 20.4 mL Q5 High-Fidelity 2X Master Mix (NEB) and 0.4 mL SuperScript II reverse transcriptase, after which it was incubated at 42°C for 15 min to fill the gaps, followed by 70°C for 15 min to inactivate SuperScript II reverse transcriptase. Next, index PCR was performed by adding 4 mL 10 mM unique dual index primers and 4 mL Q5 High-Fidelity 2X Master Mix, and thermal cycling was performed at 98°C for 30 s, followed by 18 cycles at 98°C for 20 s, 60°C for 20 s, and 72°C for 2 min, with a final step at 72°C for 5 min. The PCR product was then purified using 0.8 × VAHTS DNA Clean Beads (Vazyme).

The meta-transcriptome libraries were further enriched using biotinylated RNA/cDNA probes targeting the whole viral genome (iGeneTech, Beijing, China). The library was first quantified for the N gene using quantitative PCR after a 1:200 dilution. Next, 8 to 16 libraries were pooled together based on qPCR results. The pooled library was further processed with a TargetSeq One Cov Kit (iGeneTech) following the manufacturer's instructions. The iGeneTech Blocker was replaced by IDT xGen Universal Blockers (NXT). The final viral-enriched libraries were sequenced on an Illumina NextSeq500 platform in 2 × 75 bp paired-end mode.

Sequencing analysis of the viral genome

Quality control and error correction were implemented as previously reported (Ni et al., 2018). To avoid nucleotide-specific substitution errors in each read, we removed low-quality bases at the ends of reads with a threshold of Q20 and a minimum read length requirement of 50 bp. Reads without their corresponding paired reads were disregarded. The remaining paired reads were used as clean reads.

High quality viral genomic data were selected for iSNV analysis. We firstly mapped clean read data to the Wuhan-Hu-1 reference genome (GenBank accession no. NC_045512.2) using Bowtie2 v2.1.0 (Langmead and Salzberg, 2012) with default parameters and obtained 4.11 Mb (QRI: 0.44–22.96 Mb) high-quality viral reads per sample. After removing low-quality genomic data, we obtained 402 samples with sufficient data that met the following criteria: (i) sequencing depth ≥1 and reference coverage ≥50%, and (ii) depth ≥100 and reference coverage ≥10%.

iSNV calling to avoid sequencing errors and contaminants

Calling of iSNVs was performed as previously described, but with different parameters (Ni et al., 2016). Briefly, (1) sequencing reads were paired-end aligned to the reference genome sequence and reformatted using SAMtools v1.3.1 (Li et al., 2009); (2) for each site of the SARS-CoV-2 genome, aligned low-quality bases and indels were excluded to reduce the potential for false-positive results, and the site depth and strand bias were re-calculated; (3) samples with more than 3,000 sites with a sequencing depth ≥100× were selected as candidate samples for iSNV calling.

Several criteria were used to ensure high-quality iSNVs: (1) minor allele frequency ≥5% (a conservative cut-off based on error rate estimation), (2) depth of the minor allele ≥5, and (3) strand bias of the minor allele less than 10-fold or no significance detected located in one strand (Fisher's exact test for the major allele and minor allele). To avoid errors from read mapping, serial adjacent iSNVs (distance <50 bp) containing >5 iSNVs were also filtered. (4) PCR duplicate were removed with Picard MarkDuplicates, and all iSNV sites should be observed in the dataset after removing PCR duplicate.

Sequencing errors, and potential contaminants from metagenomic sequencing are significant concerns associated with next-generation sequencing. To effectively detect contaminants and sequencing errors, we performed several procedures and tests. (1) Negative control samples from healthy cases were tested to determine the potential for false-positive results. (2) The iSNV patterns from each round were carefully examined, and similar iSNV patterns were not observed in different rounds. (3) The nucleotide statistics for each site showed that we detected only 12/7037 iSNVs containing three polymorphic states, indicating that few sequencing errors occurred.

Validation of iSNVs by sample re-sequencing and PCR validation

To validate the reproducibility of the iSNVs data, we prepare two independent libraries in 62 of 402 samples. Among them, 55 samples met the criteria for iSNV calling (sequencing depth >100x, and >10% coverage). Under the 5% cut-off for mutation allele frequency (MuAF), we identified 498 iSNVs and 525 iSNVs in the first and second experiments, respectively. Over 90% (450) of iSNVs identified in the first round of sequencing were also observed in the second round (Figure S7A). The MuAFs in the two experiments were similar and highly correlated (R-square, 0.89; Figure S7B).

We also estimated the proportion of shared iSNVs under MuAF cutoff thresholds of 0.1%, 1%, 5%, 10% and 20% (Supplementary Data Table S8). We set the iSNVs identified in the second round but not in the first round as false positive mutations. The false positive rate is defined as the ratio of number of false positive mutations and iSNV numbers identified in the first round.

We also test if the reproducibility is affected by Ct value. We plot the false positive rate against the Ct value and time post-symptoms onset. Result showed that our validation on mutations was robust in reproducibility with viral load and disease process (Figure S7C, Figure S7D).

Ten PCR primer-pairs were designed for 12 genomic sites (337, 3429, 6195/6268, 7468, 10074, 18512, 17119/17318, 17812, 21711 and 23731). The primer sets are listed in the Supplementary Data Table S9. Limited by the efficiency of primers and the quality of the samples, we obtained positive PCR results for 10 genomic sites for 8 patients (16 samples). Further Sanger sequencing indicated that 7 genomic sites had mutants or iSNVs in these samples.

Correlation of iSNV density and Ct value

To test if the difference of observed number of iSNVs were due to false positive in low viral load samples, we plot the iSNV numbers to Ct value and found that iSNV richness slightly decreased with higher viral load, consistent with the previous report (Popa et al., 2020) (Figure S7E). We corrected the iSNV per KB by Ct value with linear model (Figure S7F), and observed the same increase trend over time after correction (Figure S7G).

Negative control sample in sequencing

To determine the potential false positive result, we sequenced 95 negative control samples from 31 individuals, including 40 pharyngeal swab, 15 sputum and 40 faeces. We obtained 1502 reads mapped to the SARS-CoV-2 genome in median for the negative control sample. All of the negative control sample did not meet the crania of complete genome (consensus genome >50% and deep sequencing genome >10%) (Figure S7H). The reads mapped to the SARS-CoV-2 genome showed significant difference in the negative control vs. high and low coverage samples (Figure S7I).

Normalised iSNVs and mutation rate estimation

The number of iSNVs for each sample was normalised by the number of iSNVs per kb, with only the region used to identify iSNVs used for calculation. The iSNV sites were identified throughout the genome by removing duplicated iSNVs in each patient, ensuring that iSNVs in different samples from each patient were only counted once. We also applied linear regression to evaluate the correlation between iSNVs and the time after the initial case reported, as well as the correlation between iSNVs and individual infection time of each patient.

We defined minor allele frequency (minor AF) as the allele frequency of the minor allele, whether a reference allele or alternative allele, representing a potential substitution in each individual. Mutation allele frequency (MuAF) was defined as the ratio of alternative alleles and total alleles, representing the substitution in an outbreak. We estimated the number of mutations (m) based on different mutation rate frequencies (a). According to the Bozic model (Bozic et al., 2016), the expected number of mutations was calculated using the following formula:

$$\mathrm{m} = \frac{u(1-a)}{\left(1-\frac{b}{d}\right)a}$$

where μ represents the mutation rate per genome per replication cycle, *b* represents the virus reproduction rate, and *d* represents the rate of virus decline in the population. We applied a generalised linear model to calculate the parameters and plotted the predicted values. The SARS-CoV-2 virus reproduction and decline rates *b* and *d* were not clear at the time of the study. Therefore, for comparisons of mutation rates, the numbers of expected mutations with different mutation rates were calculated using the virus reproduction and decline rates reported for influenza virus (Beauchemin and Handel, 2011; Xue et al., 2018).

Simulation of the iSNV mutation position distribution was performed with the runif function in the R using a uniform distribution with the number of iSNVs as parameters. We then ranked the actual iSNVs and simulated positions, after which we calculated the genomic distance between pairs of neighbouring mutants. The genomic distance between pairs of simulated iSNVs followed the Poisson distribution.

iSNV functional and epidemiological annotation

The iSNVs were annotated by Perl scripts and compared with the genomic annotation file of reference genome Wuhan-Hu-1 (NC_045512.2) from the NCBI. Public SNP files were downloaded from the 2019nCoVR public database (Song et al., 2020; Zhao et al., 2020a) (https://bigd.big.ac.cn/ncov/variation/annotation) on November 19 2020, yielding whole genome sequences from CNGBdb, GenBank, GISAID, GWH and NMDC. To better understand the frequencies of SNPs that occurred in populations, each iSNV was compared with the levels of SNPs according to the frequency in 2019nCoVR during the same period of sampling. Levels I to III were set according to previous definitions in public databases, where level I represents a frequency >0.05, level II represents a frequency between 0.01 and 0.05, and level III represents a frequency <0.01. The iSNVs not present in public databases were assigned to level IV. Ka and Ks were calculated by KaKs_Calculator (Wang et al., 2010) (version 2.0, June 2009 2020) using the MYN model (Zhang et al., 2006), taking the rates of transitional and transversional substitution as well as codon frequency bias into consideration. The Ka/Ks ratio has an expected value of 1 for neutral evolution.

Epitope region prediction

Predicted epitope regions were downloaded from the IEDB database (https://www.iedb.org/) (Dhanda et al., 2019), with 'Epitopes' set to 'Linear Epitope', 'Organism' set to 'SARS-CoV-2' and 'Host' set to 'Human'. Detailed epitope regions and sequences are provided in the Supplementary data (Table S10). We also explored the experimental epitope regions with the same parameters as the predicted epitopes, but with two different parameters: 'Epitopes' set to 'Any' and 'Assay' set to 'B Cell Assays: neutralisation |biological activity'.

Identifying highly correlated iSNVs in the genome by phasing analysis

Pairwise phasing analysis was performed for adjacent iSNVs (distance <50 bp) as previously reported (Chen et al., 2018). For a given pairwise iSNV, reads harbouring both positions were extracted from the alignment (SAM file). Reads with both sites mutated were designated as phased reads, and those with only one site mutated were designated as non-phased reads. Reads with a ratio of phased to non-phased reads >0.9 were selected as phased iSNVs. Moreover, the phased alternative iSNV allele frequency was required to be >0.05. For phased iSNVs in a given protein codon, we re-annotated the iSNVs with phased alleles.

Despite the short distance (<50 bp) in the genome, the correlations between long-distance (>50 bp) pairwise iSNVs were calculated by the linear adjusted R-square of variation. iSNVs were considered to be highly correlated and potentially linked if they were identified in at least three samples and possessed highly correlated MuAFs (>0.6).

S protein structure analysis and molecular dynamics simulation

All molecular dynamistic (MD) simulations were performed using the AMBER 20 package. The crystal structure of the binary complex of hACE2 and RBD (PDB ID 6LZG) (Wang et al., 2020) was used as the initial structure in the MD simulation. The protein was modelled with the AMBER FF14SB (Maier et al., 2015) all-atom protein force field and solvated by a truncated octahedron TIP3P (Jorgensen et al., 1983) water box, in which the boundary was at least 11 Å from any protein atoms. The solvated protein was neutralised and filled with 0.13 M KCl salt. In these simulations, the SHAKE (Ryckaert et al., 1977) algorithm with a relative geometric tolerance of 10^{-5} was used to constrain all chemical bonds. Mass repartitioning was applied to adjust the mass of the heavy atom to which the hydrogen was attached so that the total mass remained constant. Thus, all dynamics utilised a 4 fs time step. Long-range electrostatics were treated using the particle-mesh Ewald (PME) (Darden et al., 1993) method with default settings, and a 9 Å direct space non-bonded cutoff was used in all simulations. The system was first subjected to 10,000 steps of minimisation, after which it was gradually heated to 300 K under constant volume conditions in 1 ns. After another 5 ns of simulation using the constant isothermal-isobaric ensemble at 1 atm and 300 K, each system was equilibrated for an additional 10 ns. A Monte Carlo barostat and a weak-coupling thermostat were used. The MD simulations were performed for 300 ns with coordinates recorded every 10 ps. The same procedure was followed for simulations of the CB6 antibody (Shi et al., 2020) and the RBD complex (PDB ID 7C01 and 7BWJ). Nine RBD mutants (V407L, N422K, L452Q, E471K, V483F, G485V, Q493H, Q498H and Y505C) bound to either hACE2 or CB6 were also simulated. Simulations of these systems were performed with the procedure described above. In the analysis of simulation trajectories, hydrogen bonds were defined as a geometry with a cut-off length of 3.5 Å between the two heavy atoms of the hydrogen bonding donor and acceptor, and an X-H· · ·Y (X and Y represent heavy atoms) angle cutoff of 135°. A hydrogen bond was counted when the distance between X and Y was less than 3.5 Å and the X-H· · ·Y angle was greater than 135°.

Packaging of pseudoparticles bearing the SARS-CoV-2 spike protein and its variants

The codon-optimised S gene of SARS-CoV-2 (NC_045512.2) was incorporated into the pSecTag2/Hygro A plasmid and used as a template to generate S mutants by site-directed mutagenesis. The various S protein pseudoviruses bearing luciferase reporter genes were packaged as reported previously (Zhao et al., 2020b). In brief, 24 h prior to transfection, 293T cells were plated at a density of 6×10^5 cells per well in 6-well plates. All transfections used 4 μg plasmid DNA with 6 μL TurboFect transfection reagent (Thermo Fisher) in 400 μL Opti-MEM (Gibco). Single-cycle HIV-1 vectors pseudotyped with SARS-CoV-2 S protein, either reference protein or mutants, were produced by transfection of either HIV-1 pNL4-3 Δenv Δvpr luciferase reporter plasmid (pNL4-3.Luc.R-E-) in combination with the indicated S protein expression plasmid at a ratio of 4:1. Viral supernatants were harvested at 48 h and 72 h post-transfection, centrifuged to remove cell debris, and filtered through a 0.45 μm filter unit (Sartorius). A Lenti-X p24 rapid titre kit (Takara) was used to quantify the viral titres following the manufacturer's instructions.

Generation of cell lines expressing hACE2 and virus infectivity assay

The T Rex 293 hACE2 cell line, which expresses human ACE2 in a tetracycline-dependent manner, was established previously (Zhao et al., 2015). In brief, Flp-IN T Rex cells were plated at a density of 5×10^5 cells per well in a 6-well plate. The next day, the plated cells were cotransfected with a pcDNA5/FRT-derived human ACE2 expression plasmid and pOG44 (Invitrogen) at a molar ratio of 1:1. Two days after transfection, the transfected cells were trypsinised and reseeded at less than 25% confluence. The hACE2 cDNA-integrated cells were selected with 250 μg/mL hygromycin and 5 μg/mL blasticidin. Two weeks later, separate colonies appeared, and the pool of cells was expanded to generate cell lines that expressed hACE2 (T Rex 293 hACE2) upon the addition of tetracycline to the culture medium at a concentration of 1 μg/mL.

T Rex 293 hACE2 cells transfected with the pCAGGS-TMPRSS2 plasmid were seeded in a 96-well plate at a concentration of 2×10^4 cells per well and cultured for 12 h upon the addition of tetracycline (1 μg/mL). Using an HIV-1 p24 antigen quantification assay, we normalised the amount of pseudotyped virus particles (10 ng of p24). After normalisation, 100 μL of pseudotyped virus at a 10-fold dilution was added to each well of a 96-well T Rex 293 hACE2/TMPRSS2 culture plate, which was incubated at 37°C in a humidified atmosphere with 5% CO_2. The culture medium containing 2% foetal bovine serum (FBS) was refreshed after 12 h, and cells were incubated for an additional 48 h. Assays were performed using a luciferase assay system (Promega), and the relative light units (RLU) were read on a Promega GloMax Luminometer. Three to seven independent experiments were conducted with triplicate samples.

CB6 mAb neutralisation assay

For the neutralisation assay, T Rex 293 hACE2 cells transfected with the pCAGGS-TMPRSS2 plasmid were seeded in a 96-well plate at a density of 2×10^4 cells per well and cultured for 12 h upon the addition of tetracycline (1 μg/ml). A 100 μl volume of supernatant containing pseudoviruses was incubated with an equal volume of five-fold serially diluted antibodies for 1 h at 37°C. CB6 mAbs were tested at concentrations ranging from 0.64 ng/ml to 10.00 μg/ml. The mixtures of pseudoviruses and CB6 mAbs were then added to T Rex 293 hACE2/TMPRSS2 cells in a 96-well plate in duplicate. After a 12 h incubation, the medium was replaced with DMEM containing 2% FBS and samples were incubated for an additional 48 h at 37°C. Luciferase activity was measured using a GloMax 96 Microplate luminometer (Promega). The titres of CB6 mAbs were calculated as the 50% inhibitory concentration (IC50) using GraphPad Prism 6.0.

QUANTIFICATION AND STATISTICAL ANALYSIS

Continuous variables were expressed as median and interquartile range (IQR) values as appropriate. Categorical variables were summarised as the numbers and corresponding percentages in each category. The distribution of distance between adjacent iSNVs and expected Poisson model were performed by Kolmogorov-Smirnov test. The distance of mutations frequency under neutral selection and real frequency were performed by linear model. The distribution of codon positions was compared with the normal distribution using the Kolmogorov-Smirnov test. The correlations between iSNVs and age, gender, illness severity and viral shedding time were assessed by the Kruskal-Wallis test. The accumulation rate difference among different patient groups were performed by ANOVA linear model test. Only sites at which iSNVs occurred in more than six patients were included in the analysis. The significance of the correlations between the proportions of the population with iSNVs and hfSNPs in public databases was calculated by Fisher's exact test.